Excitation strengths and transition radii differences of one-phonon quadrupole excitations from electron scattering on ^{92,94}Zr and ^{94}Mo

Vom Fachbereich Physik
der Technischen Universität Darmstadt

zur Erlangung des Grades
eines Doktors der Naturwissenschaften
(Dr. rer. nat.)

genehmigte

D i s s e r t a t i o n

angefertigt von

Dipl.Phys. Abdulrahman Scheikh Obeid
aus Damaskus/Syrien

Referent:	Professor Dr. rer. nat. N. Pietralla
Koreferent:	Professor Dr. rer. nat. P. von Neuman Cosel
Tag der Einreichung:	21. 05. 2013
Tag der Prüfung:	19. 06. 2013

Darmstadt 2014
D 17

Zusammenfassung

Im Rahmen dieser Arbeit werden Elektronenstreuexperimente an Anregungen in ^{92}Zr und ^{94}Zr bei niedriger Energie in einem Impulsübertragsbereich $q = 0.3 - 0.6$ fm^{-1} am S-DALINAC durchgeführt. Die Natur der Einphonon-symmetrischen und -gemischtsymmetrischen 2^+ Zustände in ^{92}Zr wurde durch einen Vergleich mit Vorhersagen des Quasiteilchen-Phonon Modells (QPM) untersucht. Theoretische (e, e') Wirkungsquerschnitte wurden im Rahmen der Bornschen Nähung für verzerrte Wellen berechnet, um den Effekt der Coulombwechselwirkung zu berücksichtigen. Die reduzierten $B(E2)$ Übergangsstärken der Einphonon-Quadrupolzustände und des Einphonon-Oktupolzustandes wurden extrahiert. Die Ähnlichkeit der Impulsübertragsabhängigkeit der Formfaktoren der 2^+ Zustände bestätigt die Einphonon-Struktur des 2_2^+ Zustandes in ^{92}Zr.
Eine neue Methode basierend auf der Bornschen Nähung für ebene Wellen (PWBA) für eine modellunabhängige Bestimmung des Verhältnisses der E2 Übergangsstärken der symmetrischen (FSS) und gemischtsymmetrischen (MSS) Einphonon-Anregungen in schweren Vibrationskernen wurde entwickelt. Wegen der Empfindlichkeit der Elektronenstreuung auf Ladungsverteilungen, kann die Differenz der beiden Zustände bestimmt werden. Die Grundannahmen (Unabhängigkeit von dem Verhältnis der Coulombkorrekturen und von den absoluten Werten der Radien) wurde im Rahmen des Tassie-Modell getestet, das keine spezifischen Annahmen über die Struktur der Zustände außer der Forderung von Kollektivität des Übergangs macht. Es wird gezeigt, dass eine PWBA Analyse der Formfaktoren, die in der Regel für schwere Kerne nicht haltbar ist, in einer relativen Analyse möglich ist. Dies ist ein neuer viel versprechender Ansatz, um die Grundzustandsübergangsstärke für 2^+ MSS in Vibrationskernen mit einer Genauigkeit zu bestimmen, die nur von den experimentellen Informationen über die $B(E2; 2_1^+ \rightarrow 0_1^+)$ Stärke begrenzt ist.
Der PWBA Ansatz liefert weiterhin Informationen über die Protonübergangsradiendifferenz der jeweiligen Zustände und damit unabhängige Informationen über den gemischtsymmetrischen Charakter von 2^+-Zuständen und die Vorzeichenwechsel der dominanten Valenzschalenkomponenten zwischen FSS und MSS. Für ^{92}Zr ist die Protonenübergangsradiendifferenz im Rahmen eines Fehlers von etwa 0.5 fm mit Null verträglich. Dies ist in Übereinstimmung mit Vorhersagen, dass in diesem Fall die Neutronenkomponente einen Vorzeichenwechsel zeigt. Die

extrahierte $B(E2)$ Stärke des Übergangs in den 2_2^+ Zustand in ^{94}Zr ist kleiner als der $B(E2)$ Wert des 2_1^+ Zustandes im Gegensatz zu einer früheren, aber in Übereinstimmung mit einem neuen (n,n$'\gamma$) Experiment. Die Übergangsradiendifferenz in ^{94}Zr von $-0.24(34)$ fm ist mit Null verträglich.

Eine Analyse von zusätzlich verfügbaren Daten in ^{94}Mo zeigt, dass die Impulsübertragsabhängigkeit der Coulombkorrekturen zu einem Unterschied von mehr als 10% zwischen dem niedrigsten und dem höchsten gemessenen Impulsübertrag führt. Wenn dies mit Hilfe des Tassie-Modells korrigiert wird, erhält man einen von Null verschiedenen Wert der Übergangsradiendifferenz $\Delta R = -0.13(5)$ fm. Dies kann als Zeichen einer größeren Amplitude der führenden Proton-Zweiquasiteilchenkomponente in der Wellenfunktion des gemischtsymmetrischen 2^+ Zustandes interpretiert werden. Das $B(E2)$-Verhältnis für ^{94}Mo, 0.193(1), unterscheidet sich von dem Literaturwert, 0.138(2).

Summary

In the framework of this thesis electron scattering experiments on low-energy excitations of ^{92}Zr and ^{94}Zr were performed at the S-DALINAC in a momentum transfer range $q = 0.3 - 0.6$ fm^{-1}. The nature of one-phonon symmetric and mixed-symmetric 2^+ and 3^- states of ^{92}Zr was investigated by comparison with predictions of the quasi-particle phonon model (QPM). Theoretical (e, e') cross sections have been calculated within the distorted wave Born approximation (DWBA) to account for Coulomb distortion effects. The reduced strengths of the one-quadrupole phonon states and the one-octupole phonon state have been extracted. The similarity of the momentum-transfer dependence of the form factors between the 2^+ states supports the one-phonon nature of the 2^+_2 state of ^{92}Zr.
A new method based on the Plane Wave Born Approximation (PWBA) for a model-independent determination of the ratio of the E2 transition strengths of fully symmetric (FSS) and mixed-symmetry (MSS) one-phonon excitations of heavy vibrational nuclei is introduced. Due to the sensitivity of electron scattering to charge distributions, the charge transition-radii difference can be determined. The basic assumptions (independence from the ratio of Coulomb corrections and from absolute values of transition radii) are tested within the Tassie model, which makes no specific assumptions about the structure of the states other than collectivity. It is shown that a PWBA analysis of the form factors, which usually fails for heavy nuclei, can nevertheless be applied in a relative analysis. This is a new promising approach to determine the ground state transition strength of the 2^+ MSS of vibrational nuclei with a precision limited only by the experimental information about the $B(E2; 2^+_1 \rightarrow 0^+_1)$ strength.
The PWBA approach furthermore provides information about differences of the proton transition radii of the respective states, containing independent information about the mixed-symmetry character of 2^+ states and the sign change of leading valence shell components between FSS and MSS. For ^{92}Zr, the proton transition radii difference of the 2^+_1 and 2^+_2 states agree with zero within about 0.5 fm, consistent with predictions of a sign change of the leading neutron component in the wave function of the mixed-symmetry 2^+_2 state, while the leading proton components remain unchanged. The extracted $B(E2)$ strength of the transition of the 2^+_2 state of ^{94}Zr using the new method is smaller than the $B(E2)$ value of the 2^+_1 state in contrast to a previous but in agreement with a recent (n,n$'\gamma$)

experiment. The transition radii difference in ^{94}Zr is $-0.24(34)$ fm compatible with zero. Additional data available on ^{94}Mo were analyzed showing that the momentum transfer dependence of Coulomb corrections leads to a difference of more than 10% between the lowest and the highest measured momentum transfer. If corrected by the Tassie model, a transition radii difference $\Delta R = -0.13(5)$ fm differing from zero is found. This can be interpreted as a sign of an increase of the leading proton two-quasiparticle component in the wave function of the mixed-symmetry 2^+ state. The $B(E2)$ ratio for ^{94}Mo, 0.193(1), differs from literature, 0.138(2).

Contents

1 Introduction

Collectivity, isospin symmetry and shell structure are generic features of many-body quantum systems that consist of two components as e.g. protons and neutrons in the case of heavy atomic nuclei. The study of collective nuclear valence-shell excitations is a useful way to understand how these features coexist, interplay and compete. The development of predominantly proton-neutron symmetric collective nuclear structures at low excitation energies is dominated by a comparatively strong residual proton-neutron interaction that implies due to quantum-mechanical orthogonality the formation of further excited nuclear states with, at least partial, antisymmetry with respect to the contribution of proton and neutron valence-space components to their wave functions. Such excited states are said to have mixed symmetry [1]. The investigation of mixed-symmetry states (MSSs) is an important source of information on the effective proton-neutron interaction in the valance shell of heavy atomic nuclei [2].

The proton-neutron interactions in the nuclear valence shell and the existence of isovector valence shell excitations have been discussed in an early paper by Faessler [3] within the collective model. MSSs have been defined in the framework of the proton-neutron version of the Interacting Boson Model IBM-2 of Arima et al. [1]. The properties of a deformed nucleus in which protons and neutrons are described as identical rigid rotors have been studied by Lo Iudice and Palumbo in terms of the two-rotor model [4].

The first observation of a nuclear MSSs was achieved on the deformed nucleus ^{156}Gd in an electron scattering experiment [5] by A. Richter's group at the S-DALINAC in Darmstadt. A strong $M1$ excitation to a 1^+ state at an energy of about 3 MeV, the so-called scissors mode, was observed. The scissors mode in heavy nuclei mostly does not appear as an isolated state but is fragmented over several 1^+ states that carry the total $M1$ strength. Subsequently the scissors mode has been extensively studied in electron and photon scattering experiments on deformed nuclei and interpreted in phenomenological and microscopic models [6].

Since they are predicted as a global property of nuclei, the interests in the mixed-symmetry states is not limited to the scissors mode but are also important in weakly deformed and vibrational nuclei, which are the focus of this thesis. The

first example for a weakly collective 2^+_{ms} one-quadrupole phonon state was suggested by Hamilton et al., [7] from the analysis of the $E2/M1$ multipole mixing ratios in the $N = 84$ isotons. This kind of mixed-symmetry states was predicted by Iachello [8] in the proton-neutron version of the Interacting Boson Model IBM-2 [1], in which the symmetry of a multi-boson wave function formed by N_π proton bosons and N_ν neutron bosons is quantified by the so-called F-spin. States with $F < F_{\max} = (N_\pi + N_\nu)/2$ have wave functions that contain at least one pair of proton and neutron bosons antisymmetric under the exchange of proton and neutron labels. The signatures of MSS in vibrational nuclei with $F = F_{\max} - 1$ are (i) strong $M1$ transitions to fully symmetric states (FSS) with matrix elements of about $1\mu_N^2$ and (ii) weakly collective $E2$ transitions to FSS.

A pure mixed-symmetry states predicted by the IBM-2 was identified about thirteen years ago in ^{94}Mo [9]. A large $M1$ transition strength between low-energy states of ^{94}Mo was observed and the multiphonon structure of MSS in vibrational nuclei was confirmed [9–11]. The low-lying 2^+ states of ^{94}Mo were also investigated with electron scattering experiments at the superconducting electron accelerator S-DALINAC and with proton scattering at iThemba LABS [12]. Momentum-transfer dependence of the one-phonon FSS and MSS excitation cross sections in ^{94}Mo from electron and proton scattering was compared to IBM-2 and Quasi-Particle Phonon Model (QPM) predictions [13]. Based on the microscopic model results, the structure of the one-phonon states was analyzed in terms of their main particle-hole configurations. The QPM calculations predicted the main proton and neutron components in the wave functions of the one-phonon 2^+ states to have opposite relative signs which confirmed the picture of the isoscalar character of the FSS and isovector character of the MSS. The QPM calculations provided also evidence for the collectivity of the symmetric and mixed symmetry states, thus the transition densities of the both states are concentrated at the nuclear surface.

In the neighboring even-even isotone ^{92}Zr with two neutrons outside the N = 50 closed shell and with the Z = 40 subshell closure, a stronger configurational isospin polarization [14] of the one-phonon states than in ^{94}Mo is expected. This has recently been discussed in the literature [14–17].

In this thesis a new electron scattering experiment at the S-DALINAC has been performed on the nucleus ^{92}Zr. In the first step a calculation of the momentum-

transfer dependence of the form factors for the one-quadrupole phonon states has been done in the framework of the Quasiparticle Phonon Model. The predictions of the QPM calculations support the one-phonon structure of the 2_1^+ and 2_2^+ states and confirm the predominant isocalar and isovector nature of the symmetric and mixed symmetry states respectively.

Recent work showed that the collectivity of the low-lying symmetric and mixed-symmetric quadrupole excitations in vibrational nuclei originate from the coupling of the Giant Quadrupole Resonance (GQR) to the dominant valence-space configurations located at low energies [18]. Thus, valence space approaches like the shell model and the IBM-2 cannot account for it but have to include phenomenological effective charges. The calculations within the QPM which cover the valence part ($0\hbar\omega$ shell-model space) as well as the contribution of the GQR ($2\hbar\omega$ shell-model space), allow for a systematic study of the coupling and its relevance for the formation of mixed-symmetric quadrupole phonons. One important prediction of all microscopic models is a sign change of the dominant valence neutron amplitude of the MSS of ^{92}Zr and ^{94}Mo as compared to the 2_1^+ state.

Experimental evidence stems from the observation of a difference of the respective matter-transition radii(deduced from proton scattering) while charge-transition radii (deduced from electron scattering) were found to be about equal. One of the aims of this thesis is to determine experimentally the transition radii difference between the one-phonon symmetric and mixed-symmetry excited states of ^{92}Zr.

A new method is developed which allows a direct extraction of the charge radii difference of the FSS and MSS from electron scattering data. It is based on a relative analysis using the Plane Wave Born Approximation (PWBA), which is usually not applicable in heavy nuclei, however, it is shown to hold for cross section ratios. The new method is then applied to the neighboring nuclei ^{94}Zr and ^{94}Mo to test its validity and to study the signature of the transition radii differences predicted in [18].

In this thesis, Section 2 provides a general description of the mixing between two states and some definitions in framework of the IBM-2. It gives also a brief summary of the nuclear structure model used: the QPM. The next section gives a short background to the description of the method of electron scattering. The facility at S-DALINAC and the high resolution spectrometer (Lintott) in addition to the experimental setup for the electron scattering measurements with techni-

cal details are introduced in section 4. The next section discusses data analyzing methods for electron scattering. Section 6 discusses the one-phonon structure of the symmetric and mixed-symmetry 2^+ states of ^{92}Zr. A comparison to the QPM results was used in order to extract the $B(E2)$ strengths for the two states. Section 7 introduces the new method used to make the (PWBA) applicable for heavy nuclei. The new method will also be discussed in the framework of the Tassie model. In the last section we apply the new method to the nuclides ^{92}Zr, ^{94}Zr and ^{94}Mo. The charge transition radii difference between the symmetric and mixed-symmetry states of the three nuclei are extracted. The thesis closes with a summary and outlook.

2 Theoretical background

2.1 Mixed-symmetry states

2.1.1 Two-state mixing

The nuclear many-body eigenvalue problem

$$H\psi = E\psi \tag{2.1}$$

is very difficult to solve exactly. An accurate treatment must involve the diagonalisation in a large basis that itself is a solution to a simplified Hamiltonian H_0 such that

$$H = H_0 + H_1 = (T + V_0) + V_1, \tag{2.2}$$

and H_1 is sufficiently small. The basis states φ_i are the eigenstates of H_0

$$H_0\varphi_i = E_i\varphi_i \tag{2.3}$$

If we expand ψ in terms of the basic states φ_i that are eigen functions of the operator H_0 with eigenvalues E_i the Hamiltonian equation becomes [19]:

$$\begin{bmatrix} E_1 & V_{12} & V_{13} & \cdots & V_{1n} \\ V_{21} & E_2 & V_{23} & \cdots & \\ V_{31} & V_{32} & E_3 & \cdots & \\ \vdots & & & & \vdots \\ V_{nl} & & & & E_n \end{bmatrix} \begin{bmatrix} \\ \\ \\ \varphi \\ \\ \\ \\ \end{bmatrix} = \begin{bmatrix} \\ \\ \\ E \\ \\ \\ \\ \end{bmatrix} \begin{bmatrix} \\ \\ \\ \varphi \\ \\ \\ \\ \end{bmatrix},$$

where ψ and E are column vectors whose components are ψ_i and E_i. By diagonalizing the Hamiltonian in the basis ψ the wave functions will be given by

$$\psi_k = \sum_i \alpha_i^k \varphi_i, \tag{2.4}$$

where α_i^k are the expansion coefficients for the k-th state obtained from the diagonalization. The solution is usually very complex and makes it difficult, to

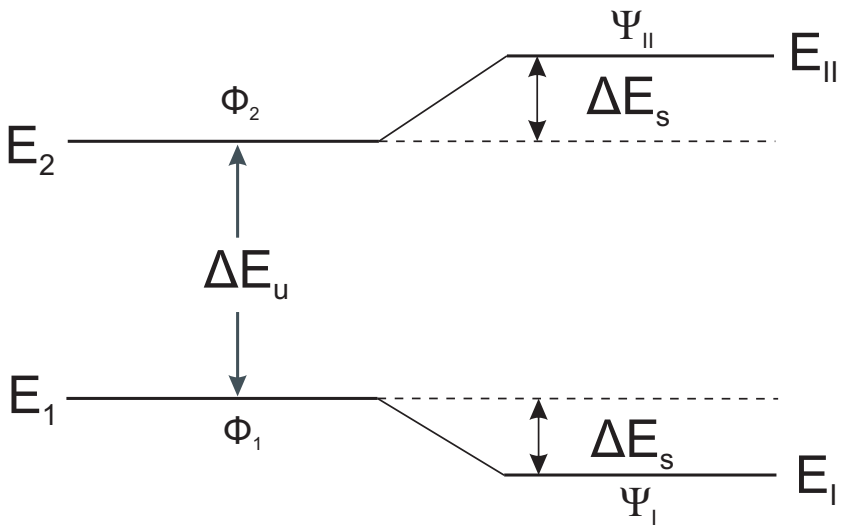

Figure 2.1: Mixing of two states with initial energy space of ΔE_u [19].

gain a feeling for the underlying physics. In order to keep sight of the basic physics we will consider a simple two-state mixing. We follow here closely the notation of Ref. [19]. Fig. 2.1 illustrates a situation in which two initial levels with energies E_1 and E_2 have wave functions ϕ_1 and ϕ_2. The two wave functions interacting with each other through the mixing matrix element $\langle \phi_1 | V | \phi_2 \rangle$, where V is negative and has attractive nature. The mixing depends on the initial energy difference and on the matrix element. The final energies $E_{\rm I}$ and $E_{\rm II}$ and wave functions $\Psi_{\rm I}$ and $\Psi_{\rm II}$ are obtained by diagonalizing the matrix

$$\begin{bmatrix} E_1 & V \\ V & E_2 \end{bmatrix},$$

and the final form of the mixed wave functions is

$$\begin{aligned} \Psi_{\rm I} =& \alpha\phi_1 + \beta\phi_2, \\ \Psi_{\rm II} =& -\beta\phi_1 + \alpha\phi_2, \end{aligned} \tag{2.5}$$

where $\alpha^2 + \beta^2 = 1$ [19]. The mixing depends both on the initial separation between the two states ΔE_u and on the matrix element, V. A large spacing between the states reduces the effect of a given matrix element and vice versa, if states are close in energy, a small matrix element may induce a large mixing. We can define the ratio

$$R = \frac{\Delta E_u}{V}, \tag{2.6}$$

which is a universal two-states mixing parameter valid for any interaction and any initial spacing. The shift in energy is then given by

$$\frac{|\Delta E_s|}{\Delta E_u} = \frac{1}{2}\left[\sqrt{1+\frac{4}{R^2}} - 1\right] \tag{2.7}$$

and the amplitude β is given by

$$\beta = \frac{1}{\left\{1 + \left[R/2 + \sqrt{1+R^4/4}\right]^2\right\}^{\frac{1}{2}}} \tag{2.8}$$

It is obvious in the Eqs. 2.7 and the mixed amplitudes 2.8 that the final energy deference and β depend only on R. This means that the same value of R always gives the same final wave functions, energies, and energy shifts independent of the nature of the interaction or the initial splitting.

2.1.2 Mixing and transition rates

It is of a interest to discuss the effect of certain types of mixing on the transition rates. In Fig. 2.2 it is supposed that the 2_1^+ state has an allowed transition to the ground state A and the 2_2^+ state has forbidden transitions to both 2_1^+ and 0_1^+ states. It is obvious in this case that the only possibility for the 2_2^+ state

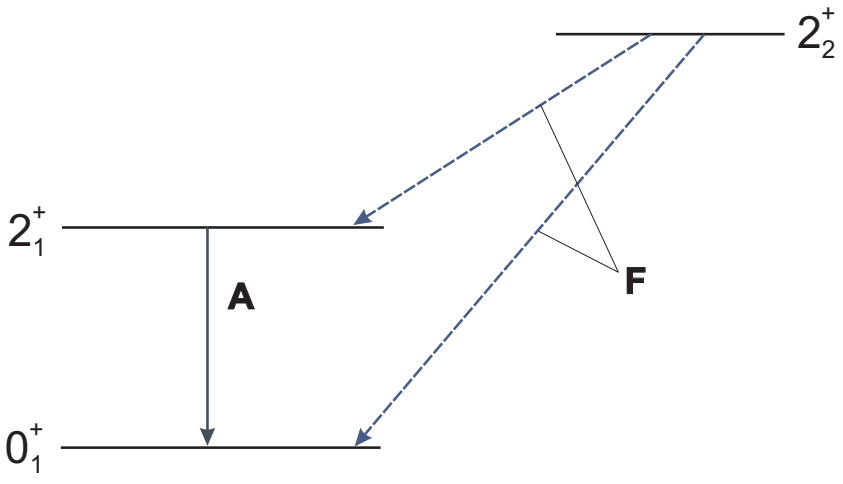

Figure 2.2: Effect of mixing on forbidden transition [19].

to make a transition to the 2_1^+ and 0_1^+ states, is to mix with the 2_1^+ state. If

the two 2^+ states mix they will share some of the same character and should be interconnected and some of the strength of the allowed transition should be distributed to the forbidden one [19]. Using the notation of Fig. 2.1 we can calculate the $\pi\lambda$ moment for the mixed states. For the second state we have

$$\begin{aligned}\left\langle 2^+_{\rm II}|\pi\lambda|0^+_1\right\rangle &= \left\langle(-\beta 2^+_1 + \alpha 2^+_2)|\pi\lambda|0^+_1\right\rangle \\ &= -\beta\left\langle 2^+_1|\pi\lambda|0^+_1\right\rangle + \alpha\left\langle 2^+_2|\pi\lambda|0^+_1\right\rangle \\ &= -\beta\left\langle 2^+_1|\pi\lambda|0^+_1\right\rangle,\end{aligned} \tag{2.9}$$

since the transition $2^+_2 \to 0^+_1$ is forbidden. Thus the $2^+_{\rm II} \to 0^+_1$ arises only from mixing with the 2^+_1 state. For the $2^+_{\rm II} \to 2^+_{\rm I}$ transition we have

$$\begin{aligned}\left\langle 2^+_{\rm II}|\pi\lambda|2^+_{\rm I}\right\rangle &= \left\langle(-\beta 2^+_1 + \alpha 2^+_2)|\pi\lambda|(\alpha 2^+_1 + \beta 2^+_2)\right\rangle \\ &= -\alpha\beta\left\langle 2^+_1|\pi\lambda|2^+_1\right\rangle + \alpha\beta\left\langle 2^+_2|\pi\lambda|2^+_2\right\rangle \\ &\quad -\beta^2\left\langle 2^+_1|\pi\lambda|2^+_2\right\rangle + \alpha^2\left\langle 2^+_2|\pi\lambda|2^+_1\right\rangle.\end{aligned} \tag{2.10}$$

Since the transition $2^+_2 \to 2^+_1$ is assumed to be forbidden, the last two terms vanish and

$$\begin{aligned}\left\langle 2^+_{\rm II}|\pi\lambda|2^+_{\rm I}\right\rangle &= -\alpha\beta\left\langle 2^+_1|\pi\lambda|2^+_1\right\rangle + \alpha\beta\left\langle 2^+_2|\pi\lambda|2^+_2\right\rangle \\ &= \alpha\beta(\left\langle 2^+_2|\pi\lambda|2^+_2\right\rangle - \left\langle 2^+_1|\pi\lambda|2^+_1\right\rangle).\end{aligned} \tag{2.11}$$

In the discussion of this result we distinguish between two cases:

1. In the case that the diagonal matrix elements of the unperturbed states $\left\langle 2^+_{1,2}|\pi\lambda|2^+_{1,2}\right\rangle$ are small, the mixed transition strength should be small also.

2. In the case that the diagonal matrix elements $\left\langle 2^+_{1,2}|\pi\lambda|2^+_{1,2}\right\rangle$ are large, we have then two extreme cases

   a) Isoscalar excitation: The two unperturbed states are supposed to be either protons or neutrons. If they have the same value of the moment $\left\langle 2^+_1|\pi\lambda|2^+_1\right\rangle = \left\langle 2^+_2|\pi\lambda|2^+_2\right\rangle = B$, then we have isoscalar excitation.

$$\begin{aligned}\left\langle 2^+_{\rm II}|\pi\lambda|2^+_{\rm I}\right\rangle &= \alpha\beta(\left\langle 2^+_2|\pi\lambda|2^+_2\right\rangle - \left\langle 2^+_1|\pi\lambda|2^+_1\right\rangle) \\ &= \alpha\beta(B - B) \\ &= 0\end{aligned} \tag{2.12}$$

   This isoscalar case applies often to E2, E3, $\cdots$ transitions, because the operators are predominantly isoscalar.

b) Isovector: If the two unperturbed states that are supposed to be either protons or neutrons, have the same value of the moment with different sign $\langle 2_1^+|\pi\lambda|2_1^+\rangle = -\langle 2_2^+|\pi\lambda|2_2^+\rangle = B$

$$\begin{aligned}\langle 2_{\mathrm{II}}^+|\pi\lambda|2_{\mathrm{I}}^+\rangle =& \alpha\beta(\langle 2_2^+|\pi\lambda|2_2^+\rangle - \langle 2_1^+|\pi\lambda|2_1^+\rangle) \\ =& \alpha\beta(B+B) \\ \langle 2_{\mathrm{II}}^+|\pi\lambda|2_{\mathrm{I}}^+\rangle =& 2\alpha\beta B\end{aligned} \tag{2.13}$$

This case often applys to E1, M1, $\cdots$ transitions.

2.2 The interacting boson model

2.2.1 s, d Bosons and Operators

The collective behavior of the low lying states can be approximated in the framework of the Interacting Boson model. This model was introduced by Arima und Iachello in 1975 [20]. The basic assumption of this model is that the low-lying collective states of medium and heavy even-even nuclei outside the closed shells are dominated by excitations of the valence protons and neutrons only, while the closed-shell core is inert [22]. Furthermore, it is assumed, due to the pairing force, that the protons and neutrons contribute as bosons in the particle configuration of the low-lying states in which identical particles are coupled together forming pairs of angular momentum 0 and 2 [21]. Proton (neutron) bosons with angular momentum 0 are called s-bosons and denoted by $s_\pi(s_\nu)$, while the proton (neutron) bosons with angular momentum 2 are called d-bosons and are denoted by $d_\pi(d_\nu)$. The nuclear states have a total number of bosons $N = n_s + n_d$, where $n_{s(d)}$ is the number of $s(d)$ bosons. These two values for angular momentum are enough for a satisfactory description of several nuclear properties and for more properties bosons with angular momenta other than 0 or 2 should be included. In order to achieve a circumstantial description of the nuclear properties a separate treatment of the proton bosons and neutron bosons is required. This is included in the proton-neutron version of the Interacting boson model which is called IBM-2. The number of the proton (neutron) bosons $N_\pi(N_\nu)$ is counted

from the nearest closed shell. If less than half of the valence shell is filled, the number of the bosons is the number of the pairs of particle, while it is the number of pairs of holes otherwise. Thus the valence protons and neutrons in medium and heavy nuclei occupy different major shells, so the contribution of proton-neutron pairs is negligible and excluded from the IBM-2 [21]. In lighter nuclei valence protons and neutrons occupy the same major shell and the proton-neutron pairs have more important contribution in the configuration of the wave function of the low-lying states. Proton-neutron pairs are included in the IBM-3 and IBM-4 [21]. The *sd*-IBM-2 can describe nuclear levels of positive parity and even-even nuclei only. In the *sd*-IBM the configuration of the states can be written in terms of the boson creation $(s^\dagger, d^\dagger_\mu)$ and boson annihilation (s, d_μ) operators

$$\begin{cases} s^\dagger_\pi, d^\dagger_{\pi,\mu}, s^\dagger_\nu, d^\dagger_{\nu,\mu}, & (\mu = 0, \pm 1, \pm 2) \\ s_\pi, d_{\pi,\mu}, s_\nu, d_{\nu,\mu}, & (\mu = 0, \pm 1, \pm 2) \end{cases} \tag{2.14}$$

and they satisfy the commutation relations

$$\left[s, s^\dagger\right] = \quad 1 \tag{2.15}$$

$$\left[d_\mu, d^\dagger_\nu\right] = \quad \delta_{\mu\nu}, \tag{2.16}$$

where $\mu = -2, -1, 0, 1, 2$ is the projection quantum number. All other possible commutators vanish. Instead of the (s, d_μ) operators $(\tilde{s}, \tilde{d}_\mu)$ are used, because the tilded annihilation operators do transform as spherical tensors under rotations, while the d_μ do not.

Schematically the Hamiltonian of the IBM-2 has the following form

$$\hat{H} = \hat{H}_\pi + \hat{H}_\nu + \hat{V}_{\pi\nu}, \tag{2.17}$$

where $\hat{H}_\pi$ and $\hat{H}_\nu$ are given in the Hamiltonian of the IBM-1 as

$$\hat{H}_\rho = E_0^{(\rho)} + \sum_{\alpha\beta} \epsilon^{(\rho)}_{\alpha\beta} b^\dagger_{\rho,\alpha} b_{\rho,\beta} + \sum_{\alpha\beta\gamma\delta} \frac{1}{2} u^{(\rho)}_{\alpha\beta\gamma\delta} b^\dagger_{\rho,\alpha} b^\dagger_{\rho,\beta} b_{\rho,\gamma} b_{\rho,\delta} + \cdots, (\rho = \pi, \nu), \tag{2.18}$$

where $b, b^\dagger$ are the boson annihilation and creation operators and $\alpha, \beta, \gamma, \delta$ codify additional quantum numbers for angular momentum, isospin, and magnetic substates [23].

$\hat{V}_{\pi\nu}$ codifies the interaction between proton and neutron bosons. It conserves

separately the number of proton and neutron bosons, as $\hat{H}_\rho$ does, which is a consequence of the microscopic structure of the bosons and originates from the conservation of the particle number.
The $\hat{H}_\rho$ can be written as

$$\begin{aligned}\hat{H}_\rho = \epsilon_\rho \hat{n}_{d\rho} + a_0^\rho(\hat{P}_\rho^\dagger \cdot \hat{P}_\rho) + a_1^\rho(\hat{L}_\rho \cdot \hat{L}_\rho) + a_2^\rho(\hat{Q}_\rho \cdot \hat{Q}_\rho) \\ + a_3^\rho(\hat{U}_\rho \cdot \hat{U}_\rho) + a_4^\rho(\hat{V}_\rho \cdot \hat{V}_\rho)\end{aligned} \tag{2.19}$$

where

$$\begin{aligned}\hat{n}_{d_\rho} &= (d_\rho^\dagger \cdot \tilde{d}_\rho), \\ \hat{P}_\rho &= \frac{1}{2}(\tilde{d}_\rho \cdot \tilde{d}_\rho) - \frac{1}{2}(\tilde{s}_\rho \cdot \tilde{s}_\rho), \\ \hat{L}_\rho &= \sqrt{10}[d_\rho^\dagger \cdot \tilde{d}_\rho], \\ \hat{Q}_\rho &= [d_\rho^\dagger \times \tilde{s}_\rho + s_\rho^\dagger \times \tilde{d}_\rho]^{(2)} - \frac{1}{2}\sqrt{7}[d_\rho^\dagger \times \tilde{d}_\rho]^{(2)} \\ \hat{U}_\rho &= [d_\rho^\dagger \times \tilde{d}_\rho]^{(3)} \\ \hat{V}_\rho &= [d_\rho^\dagger \times \tilde{d}_\rho]^{(4)}\end{aligned} \tag{2.20}$$

while the proton-neutron interaction $\hat{V}_{\pi\nu}$ requires additional operators

$$\begin{aligned}\hat{Q}_\rho^{'} &= [d_\rho^\dagger \times \tilde{d}_\rho]^{(2)} \\ \hat{Q}_\rho^{''} &= [d_\rho^\dagger \times \tilde{s}_\rho - s_\rho^\dagger \times \tilde{d}_\rho]^{(2)}\end{aligned} \tag{2.21}$$

2.2.2 F-spin

In analogy to the isospin symmetry of nucleons, the symmetry of a multi-boson wave function formed by N_π proton bosons and N_ν neutron bosons is quantified by the so-called F-spin quantum number. In this system the proton and neutron bosons (b_π, b_ν) are considered as elementary particles and have $F = 1/2$ with the z-projection $F_z = +1/2$ for the proton bosons and the z-projection $F_z = -1/2$ for the neutron bosons. The treatment of the bosons as an F-spin doublet imposes an $SU(2)$ group structure on the transformations of the proton-neutron boson basis states. For a system of s-and d-bosons only, the generators of this group

are

$$\begin{aligned}\hat{F}_+ &= d_\pi^\dagger \cdot \tilde{d}_\nu + s_\pi^\dagger \cdot s_\nu \\ \hat{F}_- &= d_\nu^\dagger \cdot \tilde{d}_\pi + s_\nu^\dagger \cdot s_\pi \\ \hat{F}_z &= \frac{1}{2}[d_\pi^\dagger \cdot \tilde{d}_\pi + s_\pi^\dagger \cdot s_\pi - d_\nu^\dagger \cdot \tilde{d}_\nu - s_\nu^\dagger \cdot s_\nu] \\ &= \frac{1}{2}(\hat{N}_\pi - \hat{N}_\nu),\end{aligned} \tag{2.22}$$

where $\hat{N}_{\pi(\nu)}$ is the total proton (neutron) boson number. $\hat{F}_+$ and $\hat{F}_-$ enhance and lower the $\hat{F}_z$ by one unit. $\hat{F}_z$ is one half of the difference between the proton and the neutron boson numbers. Analog to angular momentum operators these generators satisfy the commutation relations

$$\begin{aligned}\left[\hat{F}_z, \hat{F}_\pm\right] &= \pm\, \hat{F}_\pm \\ \left[\hat{F}_+, \hat{F}_-\right] &= 2\hat{F}_z,\end{aligned} \tag{2.23}$$

and, consequently, the boson basis states can simultaneous be eigenstates of the quadratic F-spin operator

$$\hat{F}^2 = \hat{F}_-\hat{F}_+ + \hat{F}_z(\hat{F}_z + 1), \tag{2.24}$$

and the z-component $\hat{F}_z$ of the F-spin operator with eigenvalues $F(F+1)$ and F_z, respectively. For this system the maximum F-spin is given by

$$F_{max} = \frac{N_\pi + N_\nu}{2} \geq F \geq \frac{|N_\pi - N_\nu|}{2}. \tag{2.25}$$

States with $F = F_{max}$ are the proton-neutron FSSs, while states with $F < F_{\max} = (N_\pi + N_\nu)/2$ are the MSSs and have wave functions that contain at least one pair of proton and neutron bosons antisymmetric under the exchange of proton and neutron labels [2]. Thus, the investigation of MSSs provide a better understanding of the *pn* degrees of freedom in heavy nuclei.

The IBM is a symmetry-based model which contains a vibrational and a rotational limit [24]. In the sd-IBM-2 unitary transformations among the six s, d states generates the Lie algebra $U(6)$. In the microscopic interpretation of the s and d bosons in an even-even nucleus with $2N$ nucleons, a low-lying collective state is approximated as an N-boson state. In this case the numbers of s and d bosons (n_s, n_d) are not implicitly conserved, their sum $n_s + n_d = N$ is. In the sd-IBM-2

the proton bosons span the dynamic group $U_p(6)$ and the neutron bosons span the $U_n(6)$ one, every group contains 36 generators. Considering different degrees of freedom of the proton bosons and neutron bosons is achieved by the direct product of the two groups,

$$G = U_p(6) \otimes U_n(6). \tag{2.26}$$

This group contains 72 generators. With $N_{p(n)}$ the number of proton(neutron) bosons the states span the irreducible representation of G: $[N_p] \otimes [N_n]$. The study of subalgebras allowing the exact diagonalisation of the Hamiltonian. Taking in to account only the corresponding generators of the groups $U_p(6)$ and $U_n(6)$, we generate the group $U_{p+n}(6) \subset [N_p] \otimes [N_n]$ [25]. The states can be the characterized by the two-row irreducible representation $[N-f, f]$ of $U_{p+n}(6)$, where N is the total number of proton and neutron bosons and $f = 0, 1, \cdots, \min(N_p, N_n)$ which is used in the definition of the F-spin. The possible subalgebra chains beginning with $U_{p+n}(6)$ (in the next $U(6)$) are then:

$$U(6) \supset \begin{cases} U(5) \supset SO(5) \subset SO(3) \\ SU(3) \supset SO(3) \\ SO(6) \subset SO(5) \subset SO(3) \end{cases} \tag{2.27}$$

that present three different analytical limits, the vibrational $U(5)$ [26], the rotational $SU(3)$ [27] and the γ-unstable $SO(6)$ [28]. The Hamiltonian operator with up to two-body interactions can be then expressed as a sum of Casimir-operators for every chain

$$\begin{cases} U(5) : H = \kappa_1 C_1[U(5)] + \kappa_1' C_2[U(5)] + \kappa_4 C_2[SO(5)] + \kappa_5 C_2[SO(3)] \\ SU(3) : H = \kappa_2 C_2[SU(3)] + \kappa_5 C_2[SO(3)] \\ SO(6) : H = \kappa_3 C_2[SO(6)] + \kappa_4 C_2[SO(5)] + \kappa_5 C_2[SO(3)]. \end{cases} \tag{2.28}$$

Every Casmir operator there is associated with conserved quantum numbers, because in each limit the Hamiltonian is written as a sum of commuting operators.

The analytical eigenvalue of these Hamiltonians are given as [24]

$$\begin{cases} U(5): & E(n_d,\tau,L) = \kappa_1 n_d + \kappa_1' n_d(n_d+4) + \kappa_4\tau(\tau+3) + \kappa_5 L(L+1) \\ SU(3): & E(\lambda,\tau,L) = \kappa_2(\lambda^2+\mu^2+\lambda\mu+3\lambda+3\mu) + \kappa_5 L(L+1) \\ SO(6): & E(\sigma,\tau,L) = \kappa_3\sigma(\sigma+4) + \kappa_4\tau(\tau+3) + \kappa_5 L(L+1). \end{cases} \tag{2.29}$$

For example, Figure 2.3 shows a spectrum obtained from the $U(5)$ Hamiltonian. The $F_{\max}$ states presenting the ones occur in IBM-1, while the $F_{\max}-1$ are the MSS occurring only in IBM-2. The relevant conserved quantum numbers for the $U(5)$ symmetry are the number of neutron and proton d-bosons and the angular momentum.

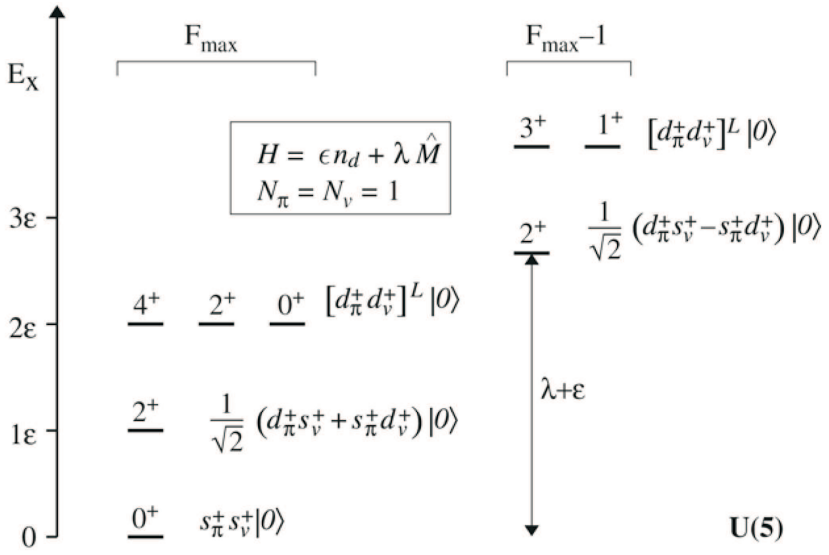

Figure 2.3: Spectrum of a schematic IBM-2 Hamiltonian with $U(5)$ symmetry with boson numbers $N_\pi = N_\nu = 1$. The boson wave functions are displayed, too. $|0\rangle$ denotes the boson vacuum and $[]^L$ denotes tensor coupling to rank L. (Taken from Pietralla et al. [2])

2.2.3 Transition operators in the IBM-2

The important signatures of 2^+ MSS are (i) strong $M1$ transitions to fully symmetric state (FSS) with matrix elements of about $1\mu_N^2$ [29], while this transition

is forbidden between the FSSs and (ii) weakly collective $E2$ transitions to FSS. Using the multipole operators in Eqs.(2.20) and (2.21) the $M1$ transition operator in the IBM-2 can be written as

$$\begin{aligned} T(M1) =& \sqrt{\frac{3}{4\pi}}[g_\pi L_\pi + g_\nu L_\nu]\mu_N \\ =& \sqrt{\frac{3}{4\pi}}[\frac{N_\pi g_\pi + N_\nu g_\nu}{N} L_{tot} + (g_\pi - g_\nu)\frac{N_\pi N_\nu}{N}(\frac{L_\pi}{N_\pi} - \frac{L_\nu}{N_\nu})]\mu_N \end{aligned} \tag{2.30}$$

where $L_{\pi(\nu)}$ denotes the angular momentum operator of isospin character and $g_{\pi(\nu)}$ is the effective proton (neutron) boson g-factor [2]. L_{tot} is the total angular momentum operator which per construction cannot induce transitions between different states and the second term can only induce $M1$ transitions between states which differ by one unit of F-spin. Thus $M1$ transitions between FSS states are forbidden. It has been shown by Van Isacker et al. [30] that for a one-body operator the equation

$$\left\langle F_{max}, j||\hat{\mathbf{T}}_\rho||F_{max}, j^{'}\right\rangle = C_{jj'}N_\rho \tag{2.31}$$

holds. For the transition between two states with the same F-spin $F = F_{max}$ we have for the second term

$$\begin{aligned} \left\langle F_{max}, I_f||\frac{\mathbf{L}_\pi}{N_\pi} - \frac{\mathbf{L}_\nu}{N_\nu}||F_{max}, I_i\right\rangle =& \frac{C_{I_iI_f}N_\pi}{N_\pi} - \frac{C_{I_iI_f}N_\nu}{N_\nu} \\ =& C_{I_iI_f} - C_{I_iI_f} \\ =& 0. \end{aligned} \tag{2.32}$$

Consequently, in the sd-IBM-2, M1 transitions are forbidden between any two FSSs. Therefore the occurrence of M1 transition strength is a unique signature for states with F-spin $F < F_{max}$, i. e., MSSs. For the $U(5)$ and $O(6)$ F-spin symmetries of IBM-2 the analytical formula of the magnetic transition strengths of the transition from the $2^+_{1,ms}$ to the 2^+_1 are given by [2]

$$\begin{aligned} B(M1; 2^+_{1,ms} \to 2^+_1)_{U(5)} =& \frac{3}{4\pi}(g_\pi - g_\nu)^2\frac{6}{N^2}N_\pi N_\nu, \\ B(M1; 2^+_{1,ms} \to 2^+_1)_{O(6)} =& \frac{3}{4\pi}(g_\pi - g_\nu)^2\frac{3(N+2)(N+4)}{4(N+1)N^2}N_\pi N_\nu, \end{aligned} \tag{2.33}$$

respectively. The $E(2)$ transition operator is given by

$$\hat{T}(E2) = e_\pi\hat{Q}^{\chi_\pi}_\pi + e_\nu\hat{Q}^{\chi_\nu}_\nu \tag{2.34}$$

with

$$\hat{Q}^{\chi_\rho}_\rho = s^\dagger_\rho \hat{d}_\rho + d^\dagger_\rho \hat{s}_\rho + \chi_\rho [d^\dagger_\rho \hat{d}_\rho]^{(2)} \tag{2.35}$$

where $e_{\pi(\nu)}$ is the effective electric quadrupole proton (neutron) boson charge. A strong $M1$ transition is an important signature of mixed symmetry states. In the F-spin symmetry $M1$ transitions between the MSSs and FSSs are proportional to the quantity $(g_\pi - g_\nu)^2 N_\pi N_\nu$. For the $U(5)$ and $O(6)$ F-spin symmetries of the IBM-2 the analytical formula of the electric quadrupole transition strengths of the transition from the $2^+_{1,ms}$ to the 2^+_1 are given by

$$\begin{aligned} B(E2; 2^+_{1,ms} \to 0^+_1)_{U(5)} =& (e_\pi - e_\nu)^2 \frac{1}{N} N_\pi N_\nu, \\ B(E2; 2^+_{1,ms} \to 0^+_1)_{O(6)} =& (e_\pi - e_\nu)^2 \frac{2(N+2)}{5N(N+1)} N_\pi N_\nu. \end{aligned} \tag{2.36}$$

Another signature of mixed symmetry states is a weakly-collective electric quadrupole transition from the MSSs to the FSSs. The $E2$ transitions in this case are as it has been shown [2] proportional to $(e_\pi - e_\nu)^2 N_\pi N_\nu$

2.3 Q-phonon coupling scheme

A special form of the IBM-2 Hamiltonian [31] for which F-spin is an exact quantum number is given by

$$H = \epsilon \, (\hat{n}_{d_\pi} + \hat{n}_{d_\nu}) + \kappa (Q^\chi_\pi + Q^\chi_\nu)^2 + \lambda (F_{max}(F_{max}+1) - \hat{F}^2). \tag{2.37}$$

In the case of nuclei that are described with structural parameters $\chi_\pi \approx \chi_\nu \approx 0$ the Hamiltonian has $O(5)$ symmetry. For a good F-spin, a discussion of the FSSs and MSSs in the IBM is more convenient in the framework of the semi-quantitative quadrupole phonon (Q-phonon) scheme, even outside of the exact dynamical symmetries. The Q-phonon scheme provides a simple tool for understanding and interpreting the complex structural mechanism in the formation of collective nuclear states. It is, therefore a very helpful formalism for the design of new experiments. The Q-phonon scheme was derived by Otsuka et al. [32]

and further developments have been achieved by the Cologne-Tokyo collaboration [31, 33–37]. In this scheme, the wave functions of low-lying collective excitations can be described as excitations by the quadrupole operators

$$\begin{aligned} \hat{Q}_s =& \hat{Q}_\pi + \hat{Q}_\nu \\ \hat{Q}_{ms} =& [\hat{Q}_\pi \frac{N}{N_\pi} - \hat{Q}_\nu \frac{N}{N_\nu}] \end{aligned} \tag{2.38}$$

where the $\hat{Q}_s$ denotes the F-scalar and result from a symmetric coupling of the proton and neutron quadrupole operators $\hat{Q}_\pi$, $\hat{Q}_\nu$ and the $\hat{Q}_{ms}$ is the mixed-symmetric quadruople operator, respectively. The fully symmetric $2^+_{1,FSS}$ state can be obtained by acting with the quadrupole operator $\hat{Q}_s$ on the ground state

$$\left|2^+_{1,FSS}\right\rangle = N_s \hat{Q}_s \left|0^+_1\right\rangle , \tag{2.39}$$

while the mixed-symmetry $2^+_{1,MSS}$ is created by acting with the quadrupole operator $\hat{Q}_{ms}$

$$\left|2^+_{1,MSS}\right\rangle = N_{ms} \hat{Q}_m \left|0^+_1\right\rangle . \tag{2.40}$$

The $2^+_{1,FSS}$ and $2^+_{1,MSS}$ have an importance in the Q-phonon scheme, because thus they are the building blocks of quadrupole collective symmetric and mixed-symmetry structures, with the N_s and N_{ms} being normalization constants. Fig. 2.4 shows the one- and two-phonon low-lying symmetric and mixed symmetric states of even-even vibrational nuclei and their experimental signature in a Q-phonon scheme [13]. Strong $M1$ transitions from the mixed-symmetry to the symmetric states is the most important signature of the one- and two-phonon mixed-symmetric states. Due to the destructive interference between the proton and neutron quadrupole phonons a weakly collective $E2$ transition from the symmetric state to the ground state is expected, while the $2^+_{1,FSS}$ is comparably strongly collective.

Following the Q-Phonon scheme higher-lying states can be clarified as multi-phonon excitations generated by coupling Q-phonons to total spin J *e.g.* the two-phonon triplet of states

$$\left|J^+_s\right\rangle \propto [\hat{Q}_s \hat{Q}_s]^{(J)} \left|0^+_1\right\rangle , \qquad \text{with } J = 0,\ 2,\ 4. \tag{2.41}$$

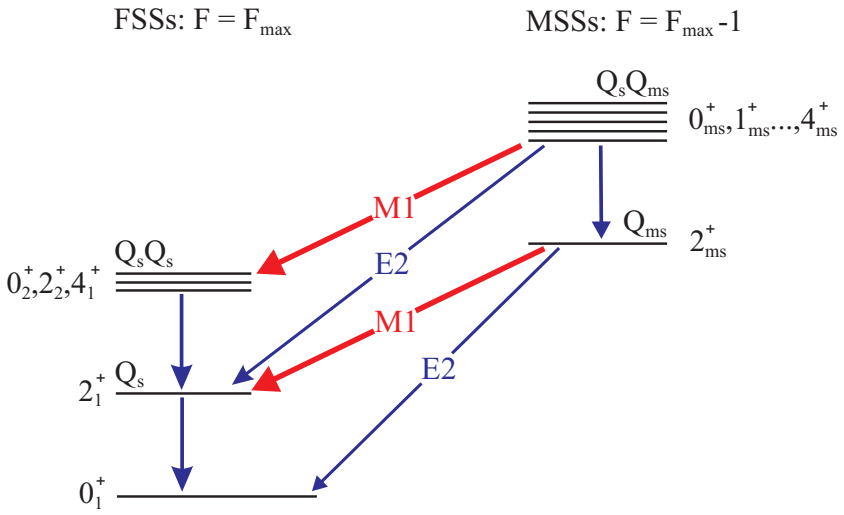

Figure 2.4: Low-lying vibrational one- and two-phonon symmetric and mixed-symmetry states in Q-phonon scheme. Strong magnetic transitions are expected between the mixed-symmetry and symmetric states resulting from the exchange between one Q_{ms}- and one Q_s-phonon and weakly collective $E2$ transitions for an annihilation of a Q_{ms}-phonon.

In terms of IBM-2 these states have an F-spin of $F = F_{max}$. For a coupling of the symmetric and the mixed-symmetric one-phonon states a quintuplet of states is formed

$$\left|J_s^+\right\rangle \propto [\hat{Q}_s \hat{Q}_{ms}]^{(J)} \left|0_1^+\right\rangle, \qquad \text{with } J = 0,\ 1,\ 2,\ 3,\ 4. \tag{2.42}$$

These states have an F-spin of $F = F_{max} - 1$.
Since the phonons Q_s and Q_{ms} are distinguishable from each other and Q_{ms} can change the F-spin quantum number at most by one unit, two-phonon states with quantum numbers 1^+ and 3^+ are allowed. The 1^+ member evolves into the scissors mode for rotational nuclei discovered in ^{156}Gd [5].
To summarize, the Q-phonon scheme shows that the annihilation and creation of the Q_{ms}-phonon leads to a weakly collective $E2$ transition to the ground state, while for the Q_s-phonon strongly collective transitions occur. In the approximation of the IBM-2, an enhanced $M1$ transition with a matrix element of the order of $1\mu_N$ results from the exchange of a Q_{ms}- and a Q_s-phonon.

2.4 The Quasiparticle Phonon Model

The Quasiparticle-Phonon Model (QPM) [38] is a microscopic model which adopts some phenomenological features of atomic nuclei. Its Hamiltonian [38–40] contains terms corresponding to an average mean field for protons and neutrons, monopole pairing, and residual nucleon-nucleon interaction. Schematically it can be written in the form

$$\hat{H} = \hat{H}_{\text{s.p.}} + \hat{H}_{pair} + \hat{H}_{r.i.}. \tag{2.43}$$

$\hat{H}_{\text{s.p.}}$, corresponds to the average field for neutrons and protons in the even even spherical nuclei. It can be written in the second quantization in terms of creation and annihilation operators as

$$\hat{H}_{\text{s.p.}} = \sum_{\tau}^{n,p} \sum_{jm} E_j a^+_{jm} a_{jm}, \tag{2.44}$$

where $j \equiv [n, l, j]$ and m, are the quantum numbers of the particles on the level of the average field and E_j is the energy of the single-particle level degenerated by magnetic quantum number m. The second term of Eq. (2.43), $\hat{H}_{pair}$ contains the residual interaction responsible for pairing in non-magic nuclei and is given by

$$\hat{H}_{\text{pair}} = \sum_{\tau}^{n,p} G^{(0)}_{\tau} \sum_{j,j'} \sqrt{(2j+1)(2j'+1)}\ [a^+_{jm} a^+_{j-m}]_{00} [a_{j'-m'} a_{j'm'}]_{00} \tag{2.45}$$

where $G^{(0)}_{\tau}$ is a constant matrix element, which assumes that monopole pairing is state-independent. With the common Clebsch-Gordan coefficient we have

$$[a^+_{jm} a^+_{j-m}]_{\lambda\mu} = \sum_{m,m'} C^{\lambda\mu}_{jmj'm'} a^+_{jm} a^+_{j'm'}. \tag{2.46}$$

The QPM is applied for studies in both magic and open shell nuclei and it has been commonly used for the description of medium and heavy nuclei. Since these nuclei have a filling of different subshells of protons and neutrons, the proton-neutron pairing is neglected. The monopole pairing strength is calculated from even-odd mass differences. We follow here closely the notation of ref. [41].

The $\hat{H}_{r.i.}$ is the residual interaction. The QPM employs the separable form of the residual interaction with Bohr-Mottelson form factor which is a derivative of the mean field. Its part in the particle hole channel can be written as

$$\hat{H}^{p-h}_{\text{r.i.}} = \sum_{\lambda\mu} \sum_{\tau\rho}^{\pm 1} (k_0^{(\lambda)} + \rho k_1^{(\lambda)}) M^+_{\lambda\mu}(\tau) M_{\lambda\mu}(\rho\tau), \tag{2.47}$$

where $k^{(\lambda)}_{0(1)}$ are the coupling parameters which determine the strength of isoscalar (isovector) residual interaction. ρ distinguish between isoscalar and isovector transitions and has the values ± 1. $M^+_{\lambda\mu}(\tau)$ and $M_{\lambda\mu}(\tau)$ are the multipole operators for natural and unnatural parity states, respectively, and given by

$$\begin{aligned} M^+_{\lambda\mu}(\tau) &= \sum_{j,m,j',m'} \left\langle jm \left| i^\lambda f^\tau_\lambda(r) Y_{\lambda\mu}(\Omega) \right| j'm' \right\rangle a^+_{jm} a_{j'm'} \\ M_{\lambda\mu}(\tau) &= \sum_{j,m,j',m',lm_1} \left\langle jm \left| i^l f^\tau_\lambda(r) \sigma . Y_{lm_1}(\Omega) \right| j'm' \right\rangle a^+_{jm} a_{j'm'} \end{aligned} \tag{2.48}$$

The value $\tau = \pm 1$ corresponds to neutrons and protons and the function $f^\tau_\lambda(r)$ is a radial form factor which in calculations is taken either in form r^λ or as a derivative of the central part of the average field for neutrons and protons $f^\tau_\lambda(r) = \mathrm{d}U^\tau(r)/dr$. In QPM this average field has the form of a Woods-Saxon potential and is given by

$$U^\tau(r) = \frac{V^\tau_0}{1 + \mathrm{e}^{(r-R^\tau_0)/a^\tau_0}} - \frac{\hbar}{\mu^2 c^2} \frac{1}{r} \frac{\mathrm{d}}{\mathrm{d}r} \left(\frac{V^\tau_{ls}}{1 + \mathrm{e}^{(r-R^\tau_{ls})/a^\tau_{ls}}} \boldsymbol{l} \cdot \boldsymbol{s} \right) + V_C(r) \tag{2.49}$$

The potential parameters are adjusted to the ground state density distribution in different A-mass regions.

The basic QPM solution of the Schrödinger equation is obtained by means of a step-by-step diagonalization of the model Hamiltonian given in Eq. (2.43). The two terms (2.44) and (2.45) are diagonalized in the first step. For this purpose Bogoliubov's canonical transformation is applied. This transformation converts the particle creation (annihilation) operators to quasiparticle creation (annihilation) operators $\alpha^+_{jm}(\alpha_{jm})$:

$$a^+_{jm} = u_i \alpha^+_{jm} + (-1)^{j-m} v_i \alpha_{j-m} \tag{2.50}$$

The ground state of even-even nuclei is considered as a quasiparticle vacuum $\alpha^+_{jm} |\rangle_q \equiv 0$. Then the energy of the ground state can be minimized using Lagrange

multiplicators and take the form:

$$\delta\left\{\left\langle\left|\hat{H}_{s.p.}+\hat{H}_{pair}\right|\right\rangle+\sum_j\mu_j(u_j^2+v_j^2-1)\right\}=0 \tag{2.51}$$

where μ_j are Lagrange coefficients. This minimization results in the well-known BCS equations

$$|BCS\rangle=\prod_{k>0}^{\infty}[u_k+v_k a_k^+ a_k^+]\,|0\rangle\,, \tag{2.52}$$

whose solutions provide the correlation functions $C_\tau = G_\tau^{(0)}\sum_j u_j v_j$ and the chemical potentials λ_τ for the neutron and proton systems. The Bogoliubov's transformation coefficients can be calculated from these values according to

$$v_2^j=\frac{1}{2}\left\{1-\frac{E_j-\lambda_\tau}{\epsilon_j}\right\},\quad u_2^j=1-v_2^j, \tag{2.53}$$

where E_j is the single-particle energy from the Wood-Saxon potential and ϵ_j is the quasiparticle energy

$$\epsilon_j=\sqrt{C_\tau^2+[E_j-\lambda_\tau]^2}. \tag{2.54}$$

The diagonalized first two terms of the model Hamiltonian given in Eq. (2.43) can be written as

$$\hat{H}_{\text{s.p.}}+\hat{H}_{pair}=\sum_\tau^{n,p}\sum_{j,m}\epsilon_j\alpha_{jm}^+\alpha_{jm}. \tag{2.55}$$

Since we have determined the ground state of even-even nuclei as the quasiparticle vacuum, the simplest excited states are two-quasiparticle states $\alpha_{jm}^+\alpha_{j'm'}^+\,|\rangle_q$. In the case that the monopole pairing vanishes, the excited states correspond to particle-hole transitions. If collective excitations are considered, this process can be described as creation of a phonon. The following phonon operator with multipolarity λ and projection μ is introduced

$$Q_{\lambda\mu i}^+=\frac{1}{2}\sum_\tau^{n,p}\sum_{jj'}\left\{\psi_{jj'}^{\lambda i}[\alpha_j^+\alpha_{j'}^+]_{\lambda\mu}-(-1)^{\lambda-\mu}\varphi_{jj'}^{\lambda i}[\alpha_j\alpha_{j'}]_{\lambda-\mu}\right\}. \tag{2.56}$$

Note that for the given multipolarity λ, the total number of different phonons (i) should be equal to the sum of neutron and proton two-quasiparticle states

coupled to the same angular momentum.
The coefficients $\psi^{\lambda i}_{jj'}$ and $\varphi^{\lambda i}_{jj'}$ can be obtained from a diagonalization of the Hamiltonian in the space of one-phonon states $Q^+_{\lambda\mu i}\left|\right\rangle_{ph}$. This can be done by applying again the variation procedure

$$\delta\left\{\left\langle\left|Q_{\lambda\mu i}\hat{H}Q^+_{\lambda\mu i}\right|\right\rangle_{ph}(w_{\lambda i}/2)\left[\sum_{jj'}\left\{(\psi^{\lambda i}_{jj'})^2-(\varphi^{\lambda i}_{jj'})^2-2\right\}\right]\right\}=0 \qquad (2.57)$$

where $w_{\lambda i}$ is the energy of the phonon i. The excitation energies of phonons and their internal fermion structure are obtained from solution of the QRPA equations under the assumption that the ground state is the phonon vacuum. The QRPA equations yield several collective phonons of different multipolarity like 2^+_1, 3^-_1, and phonons which form giant resonances and also many non-collective, or almost pure two-quasiparticle, solutions.
Excited states of even-even nuclei are considered in the QPM as phonons. The main asset of the model is that it accounts for coupling between simple (one-phonon) and complex (two-, three-phonon) configurations. A wave function of an excited state with spin and parity λ^π is written as a combination of one-, two- and three-phonon configurations. The one-phonon part of the wave function contains QRPA solutions with the fixed λ^π. The two- and three-phonon parts of it are built up from the phonons of different multipolarities which couple to the same λ^π.

The diagonalization of the model Hamiltonian on the set of these complex wave functions yields the eigenenergies and the structure of each excited state. The diagonalized matrix has a block structure. Since the Hamiltonian is already pre-diagonalized by solving the QRPA equations, one-, two-, and three-phonon parts of it are diagonal if phonons are treated as quasi-bosons. When Pauli principle corrections are accounted for, two-phonon components interact with each other as well as three-phonon components. But the largest matrix elements of interaction are between one- and two- (U^{2ph}_{1ph}) and between two- and three-phonon (U^{3ph}_{2ph}) configurations. These matrix elements are calculated microscopically from 1p3h and 3p1h parts of the residual interaction and they have finite values in both quasi-boson approximation and with accounting for the Pauli principle corrections.
The dimension of the matrix which is diagonalized equals the sum of one-, two-,

and three-phonon configurations included in the calculation. It may be reduced if necessary by excluding the complex configurations with small values of U^{2ph}_{1ph} and U^{3ph}_{2ph} matrix elements.

It should be noted that physical processes like inelastic electron scattering are often described by one-body operators. Accordingly, nuclear levels are excited predominantely via one-phonon components of the QPM wave functions. More complex configurations are responsible for fragmentation of the strength carried by these components.

3 Electron scattering

In this section some important relations for the description of inelastic electron scattering are summarized. In inclusive electron scattering experiments an electron with an incident energy E_e interacts with the current and charge density distributions of the target nuclei through virtual photon exchange. The scattered electron with energy E_f is detected at an angle θ. The excitation of the nuclei appears after neglecting the recoil energy loss of the scattered electron as $E_x = E_i - E_f$. Thus, the measurement of the energy spectrum of scattered electrons determines the excitation energy spectrum of the target nucleus. By varying the incident energy of the electron beam and/or the scattering angle one can measure the momentum transfer dependence of the squared form factor. The squared form factor is defined as the ratio of the experimental cross section to the Mott cross section for electron scattering on a massive point charge:

$$|F\left(E_i,\theta\right)|^2 = \frac{\left(d\sigma/d\Omega\right)_{\mathrm{exp}}}{\left(d\sigma/d\Omega\right)_{\mathrm{Mott}}}, \tag{3.1}$$

where the Mott cross section is given by

$$\left(\frac{d\sigma}{d\Omega}\right)_{\mathrm{Mott}} = \left(\frac{Ze^2}{2E_i}\right)^2 \frac{\cos^2\left(\theta/2\right)}{\sin^4\left(\theta/2\right)} \tag{3.2}$$

with Z being the proton number. The momentum transfer is given as

$$q_{\mathrm{x}} = \frac{1}{\hbar c}\sqrt{2E_i\left(E_i - E_{\mathrm{x}}\right)\left(1 - cos\ \theta\right) + E_{\mathrm{x}}^2} \tag{3.3}$$

and it can be written as

$$q_{\mathrm{x}}^2 = q^2\left(1 - \frac{E_{\mathrm{x}}}{E_i}\right) + \left(\frac{E_{\mathrm{x}}}{\hbar c}\right)^2 \tag{3.4}$$

where

$$q = \frac{E_i}{\hbar c}\sqrt{2\left(1 - cos\ \theta\right)} \tag{3.5}$$

is the momentum transfer of elastic scattering.
In the approximation of one-photon exchange only, the differential cross section can be written [43] using Dirac's first-order perturbation theory

$$\left(\frac{d\sigma}{d\Omega}\right) = \frac{1}{4\pi^2(\hbar c)^2} E_i E_f \left(\frac{p_f}{p_i}\right)\left(\frac{2J_f+1}{2J_i+1}\right) f_{rec}\,|\langle\psi_f|\hat{H}_{int}|\psi_i\rangle|^2, \tag{3.6}$$

where

p_i, p_f - three momentum of the electron before and after scattering,

J_i, J_f - total angular momentum of the nucleus before and after scattering,

$\hat{H}_{int}$ - the Hamiltonian interaction operator and

$f_{rec} = \left(1 + \frac{2E_i}{Mc^2} \sin^2 \frac{\theta}{2}\right)^{-1}$ - the recoil factor.

Since in the electromagnetic interaction the angular momentum and parity of the whole system are invariant, the selection rules for the angular momentum of a transition with multipolarity λ between nuclear states $|\psi_i\rangle$ and $|\psi_f\rangle$ are given by

$$|J_i - J_f| \leq \lambda \leq |J_i + J_f| \tag{3.7}$$

and for the parity

$$\pi_i \pi_f = (-1)^{\lambda} \qquad \text{for an electric transition and} \tag{3.8}$$

$$\pi_i \pi_f = (-1)^{\lambda+1} \qquad \text{for a magnetic transition.} \tag{3.9}$$

In the case of relativistic electrons and neglecting the recoil induced by the finite electron energy losses (E_i, $E_f \gg m_0c^2$, k), the differential cross section can be represented in PWBA as a sum over multipoles Eλ and Mλ, which are allowed by the selection rules discussed above [43]

$$\left(\frac{d\sigma}{d\Omega}\right) = \sum_{\lambda} \left[\left(\frac{d\sigma}{d\Omega}\right)_{E\lambda} + \left(\frac{d\sigma}{d\Omega}\right)_{M\lambda} \right]. \tag{3.10}$$

In this thesis the investigated nuclei ^{92}Zr, ^{94}Zr, and ^{94}Mo are even-even nuclei and thus have in the ground state spin and parity $J^{\pi} = 0^+$. Therefore only pure magnetic or electric transitions of the multipolarity $\lambda = J_f$ can contribute to the cross section. Thus, for an electric transition the cross section from Eq. (3.10) is reduced to

$$\left(\frac{d\sigma}{d\Omega}\right)_{E\lambda} = \left(\frac{Z\,e^2}{E_i}\right)^2 f_{rec} \left[V_L \cdot |F(C\lambda, q)|^2 + V_T \cdot |F(E\lambda, q)|^2\right] \tag{3.11}$$

and for a magnetic transition

$$\left(\frac{d\sigma}{d\Omega}\right)_{M\lambda} = \left(\frac{Z\,e^2}{E_i}\right)^2 f_{rec} \left[V_T \cdot |F(M\lambda, q)|^2\right]. \tag{3.12}$$

The functions $|F(C\lambda,q)|^2$, $|F(E\lambda,q)|^2$, $|F(M\lambda,q)|^2$ are called form factors. They are directly related to the transition matrix elements $\langle\psi_f|\hat{M}^{C\lambda}|\psi_i\rangle$, $\langle\psi_f|\hat{M}^{E\lambda}|\psi_i\rangle$ and $\langle\psi_f|\hat{M}^{M\lambda}|\psi_i\rangle$ and contain all nuclear structure information

$$\begin{aligned}
F(C\lambda,q) =& \frac{q^\lambda}{\sqrt{2J_i+1}\cdot(2J+1)!!}\,\langle\psi_f|\hat{M}^{C\lambda}(q)|\psi_i\rangle,\\
F(E\lambda,q) =& \frac{q^\lambda}{\sqrt{2J_i+1}\cdot(2J+1)!!}\sqrt{\frac{\lambda+1}{\lambda}}\,\langle\psi_f|\hat{M}^{E\lambda}(q)|\psi_i\rangle,\\
F(M\lambda,q) =& \frac{q^\lambda}{\sqrt{2J_i+1}\cdot(2J+1)!!}\sqrt{\frac{\lambda+1}{\lambda}}\,\langle\psi_f|\hat{M}^{M\lambda}(q)|\psi_i\rangle.
\end{aligned} \tag{3.13}$$

The quantities V_L and V_T depend only on the kinematics of the experiment and in the relativistic case $E_i \gg m_0c^2$ can be written as follows [43]

$$V_L = \frac{1+\cos\theta}{2(y-\cos\theta)^2}, \tag{3.14}$$

$$V_T = \frac{2y+1-\cos\theta}{4(y-\cos\theta)(1-\cos\theta)} \tag{3.15}$$

with

$$y = 1+\frac{E_x^2}{2E_i(E_i-E_x)}. \tag{3.16}$$

The reduced transition probability is related to the matrix elements Eq. (3.13) by

$$B(X\lambda,q)\uparrow = \frac{1}{2J_i+1}\,|\langle\psi_f|\hat{M}^{X\lambda}(q)|\psi_i\rangle|^2, \tag{3.17}$$

with $X = C, E$ and M, respectively. For a momentum transfer corresponding to the photon point $q = k = E_x/\hbar c$ the reduced matrix element becomes equal to that of photon excitation. In the electron scattering this value is extracted by extrapolating the measured form factor to the photon point ($q = k = E_x/\hbar c$). Using the relations (3.13) one gets for the transition components [43]

$$\begin{aligned}
B(C\lambda,q)\uparrow =& \frac{((2\lambda+1)!!)^2}{q^{2\lambda}}\,|F_\lambda^C(q)|^2,\\
B(E\lambda,q)\uparrow =& \frac{\lambda}{\lambda+1}\,\frac{((2\lambda+1)!!)^2}{q^{2\lambda}}\,|F_\lambda^E(q)|^2,\\
B(M\lambda,q)\uparrow =& \frac{\lambda}{\lambda+1}\,\frac{((2\lambda+1)!!)^2}{q^{2\lambda}}\,|F_\lambda^M(q)|^2.
\end{aligned} \tag{3.18}$$

4 Experiment at the S-DALINAC

4.1 S-DALINAC

S-DALINAC is the abbreviation for Superconducting DArmstadt electron LINear ACcelerator. It was constructed by diploma and doctoral students at the Institute of Nuclear Physics of Darmstadt Technical University [45]. Since 1991 it became the first superconducting continuous-wave linear electron accelerator in Europe and is regularly used for a wide range of nuclear physics experiments. The S-DALINAC provides electron beams with energies up to about 100 MeV and beam currents up to 10μA for several experimental facilities. Figure 4.1 shows a schematic layout of the S-DALINAC and the experimental facilities. The following description is based on [13] A thermionic gun emits electrons which are

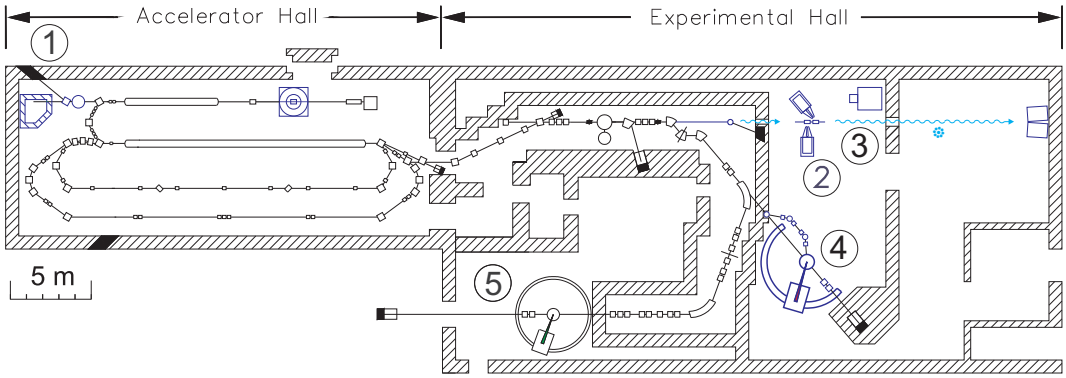

Figure 4.1: Experimental facilities at the S-DALINAC. ① Nuclear resonance fluorescence ② Polarisability of the nucleon. ③ $(\gamma, \gamma' x)$ experiments at NEPTUN tagger. ④ $(e, e' x)$ and 180° experiments at QCLAM spectrometer.⑤ High-resolution (e, e') experiments at 169° spectrometer

preaccelerated electrostatically to an energy of 250 keV. The required time structure of the electron beam for radio-frequency acceleration in a 3 GHz field is created by a chopper/prebuncher system operating at room temperature. Electron bunches leaving the chopper/prebuncher system enter the injector which consists of one 2-cell, one 5-cell, and two standard 20-cell niobium cavities cooled to 2 K by liquid helium. In the injector the electron bunches are accelerated up to

10 MeV and can be directly used for nuclear resonance fluorescence experiments at the experimental site denoted by ① in Fig. 4.1. Alternatively, they can be injected by a 180° bending system into the main superconducting linear accelerator [46], which consists of eight 20-cell niobium cavities and provides an energy increase of up to 40 MeV. After acceleration in the main linac the electron beam can either be extracted to the experimental hall or recirculated and reinjected once or twice into the main linac. After two recirculations the electron beam can be delivered to several experimental facilities with an energy up to about 100 MeV. It can be converted to bremsstrahlung photons and used for the study of the nucleon polarizability ② and $(\gamma, \gamma^{'}x)$ experiments at the low energy photon tagger NEPTUN ③ . A wide range of electron scattering experiments is carried out using the QCLAM spectrometer ④ and the high-resolution electron scattering facility with the 169° spectrometer ⑤ , the so-called Lintott spectrometer. The QCLAM spectrometer is mainly used for $(e, e^{'})$ experiments at 180° scattering [47–49] and $(e, e^{'}x)$ coincidence experiments [50–53]. It has a large angular and momentum acceptance. The present work has been executed at the Lintott spectrometer which is described in greater detail in the following section.

4.2 Lintott spectrometer and high-resolution electron scattering

Lintott is the name of the 169° spectrometer spectrometer which is used for the high resolution electron scattering experiments. It is shown in Fig.4.2. The electron beam comes from the left side ① and hits the target which is placed in the center of the scattering chamber ② . After the interaction with the target nuclei, the scattered electrons passing through the spectrometer's entrance slit defining the solid angle Ω are deflected by the dipole magnet ③ and focused to the focal plane of the spectrometer ④ . The electrons in the central trajectory are bent to an angle of 169.7°, the so-called "magic" angle [54] which is chosen to improve the ion-optical properties of the spectrometer summerized in Tab. 4.1. When the beam is focused on the small area of the target (conventional mode), the energy resolution of the Lintott spectrometer depends mainly on the energy

spread of the primary electron beam, which is $\Delta E/E \approx 10^{-3}$. Because of the energy spread ΔE of the beam, the scattered particles which have excited the same level will leave the target with slightly different energies and therefore will hit the detector plane at slightly different places according to the energy spread of the particles beam ΔE. This will affect the energy resolution of the spectrum. This energy resolution is sufficient to perform experiments with light nuclei where the level densities are not very high but for heavy nuclei a high-resolution mode is needed.

Figure 4.2: View of the Lintott spectrometer. The electron beam ① comes from the left side and hits the target which is placed in the scattering chamber ② . The scattered electrons pass to the spectrometer entrance and are deflected by the dipole magnet ③ and focused to the focal plane of the spectrometer ④

Table 4.1: Main parameters of spectrometer.

Electron energy range	$1.5 \cdot 10^{-4}$
Energy resolution	$20 - 120\,\mathrm{MeV}$
Angle range	$33^\circ - 165^\circ$
Angle step	12°
Deflection angle	$169.7^\circ \pm 0.1^\circ$
Dispersion	3.76 cm/%
Momentum acceptance	$\pm 2.1\%$
Resolution (point source, FWHM)	0.015 %
Maximal solid angle acceptance	6 msr

In order to increase the energy resolution of the spectrometer the lateral dispersion matching technique (often called „energy-loss mode“) is used. The basic principle of lateral dispersion matching is to match the adjusted beam dispersion, emittance and spot size at the target position with the ion-optical properties of the spectrometer.

In the lateral dispersion matching mode the electron beam is projected on the target by the beam transport system on a narrow line which is vertical to the plane determined by the incoming and scattered beam, while the beam is focused in non dispersive direction. Its size corresponds to the beam energy spread ΔE (see Fig.4.3). The dispersion of the beam at the target is adjusted to the electron optics of the spectrometer in such a way that the trajectories of different momenta through the magnetic field have different path lengths such that they focus back on the focal plane at one spot. In this case one gets a better image resolution which is almost unaffected by the energy spread of the primary beam. If the electrons excite the nuclei to an excited state, they loose some energy δE and the beam spot in the focal plane of the detector system is displaced by a distance determined by the excitation energy of that state. This makes the energy resolution independent of the energy spread of the beam and makes the system sensitive only to the energy loss in the target. The relative energy resolution achieved with such a technique is down to $\Delta E/E \approx 3.10^{-4}$.

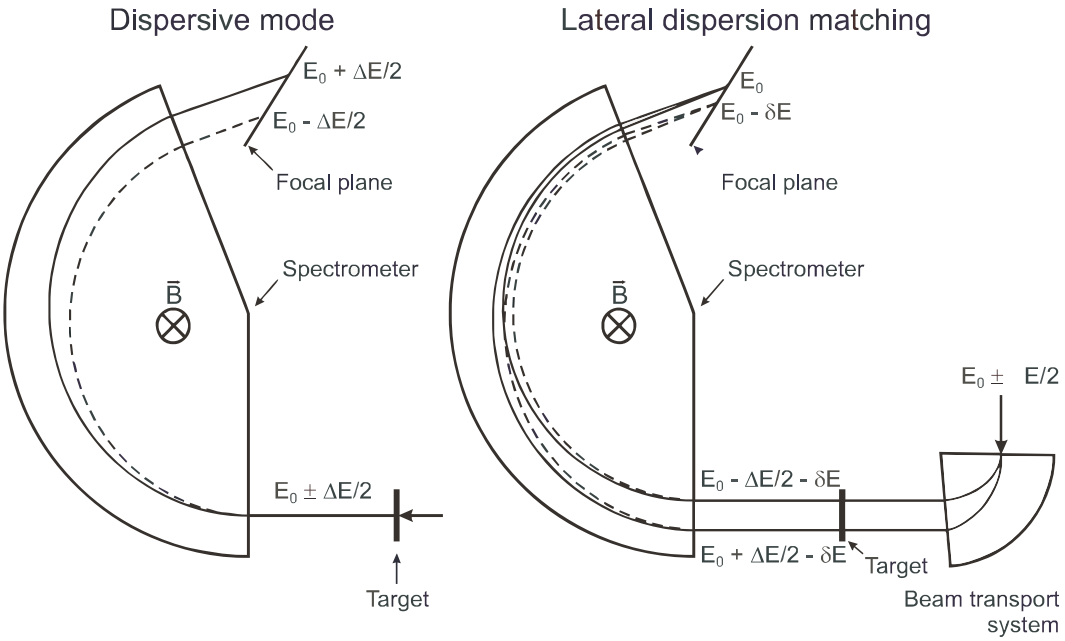

Figure 4.3: The position and the angle of scattered particles at the focal plane depend on the initial energy spread in the dispersive mode, left, which thereby limits the resolution. Lateral dispersion matching allows to improve the resolution by spatially spreading the beam spot at the target position according to the dispersion of the beam, matching it to that of the spectrometer. (Taken from Burda et al., [13]).

4.3 Detector system

Electron scattering experiments have been successfully performed for many years using the magnetic 169° spectrometer (Lintott) with a focal plane detector system based on overlapping scintillators [54–57]. However, the plastic scintillators have some significant drawbacks like different individual detection efficiency such that lengthy repetitions of the measurements are required. Recently, an improvement of the complete beam line for dispersion matching [58] together with the vacuum system, focal plane detection system [59, 60] and its background shielding was performed [61].

The new detector system consists of silicon microstrip detectors and a trigger detector. Figure 4.4 presents a photograph of the silicon microstrip detector system. Because of difficulties to grow Si crystals of the requested size there is no single detector plate available covering the full focal plane length of 24 cm.

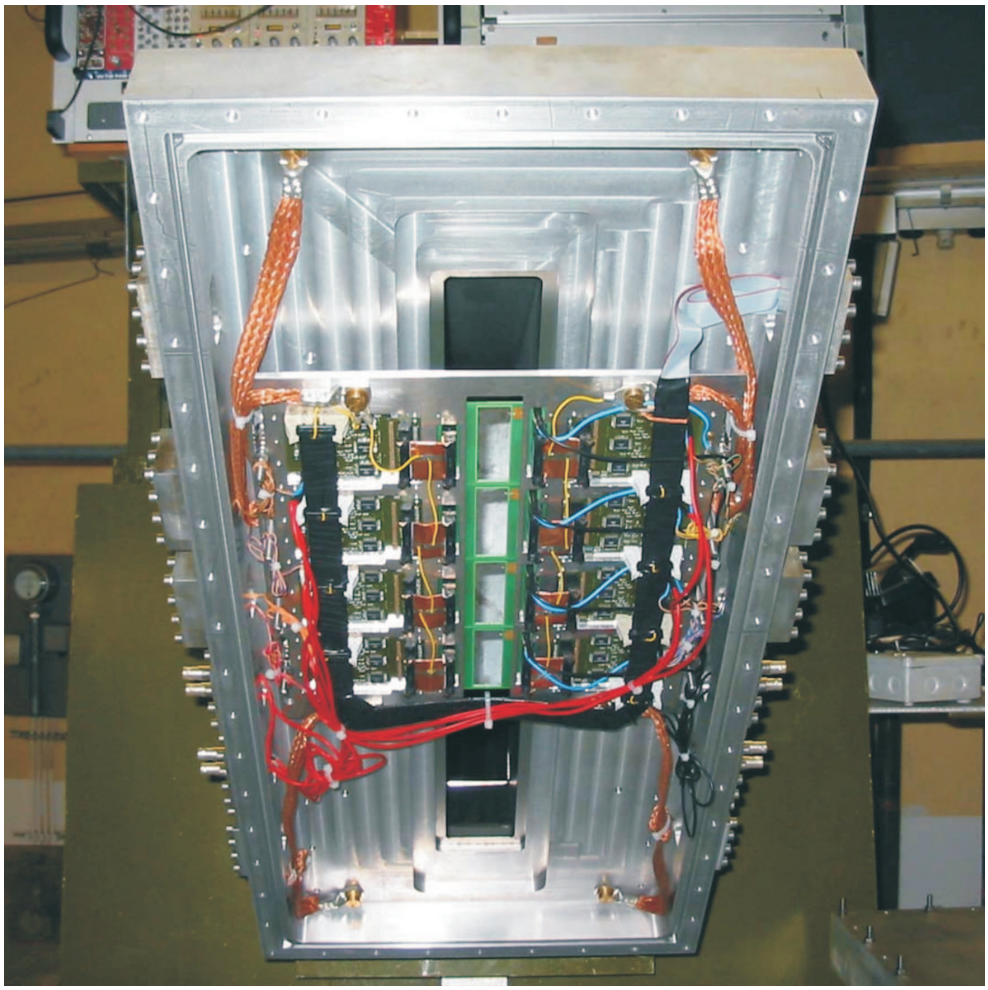

Figure 4.4: A photo of the silicon strip detector system mounted in the magnetic spectrometer

Therefore, four detector plates were mounted together separated by an inactive zone of about 7 mm between two adjoining detectors, each plate providing 96 strips with a thickness of 500 μm and a pitch of 650 μm. The trigger detector system consists of a 40 cm long plastic scintillator with a thickness of 5 mm (material NE102A) and a 40 cm long Cherenkov counter of 5 cm thickness run in coincidence. It is used for background suppression and is placed outside the vacuum chamber. The new detector system has a high spatial resolution (1.5×10^{-4}) due to the small thickness of its silicon microstrip and has the ability to process very high count rates (100 kHz), because of the simple readout.

4.4 Experiments

The experiments have been carried out at the Darmstadt superconducting electron linear accelerator S-DALINAC. The high-resolution spectrometer Lintott with its detector system was used. Measurements were performed on the nuclides ^{92}Zr and ^{94}Zr. For ^{92}Zr the incident beam energy was $E_0 = 63$ MeV with beam currents ranging from 0.5 to 1 μA. A ^{92}Zr target with an isotopic enrichment of 94.57% and a thickness of 9.75 mg/cm^2 was used. Data were taken at five different scattering angles $\theta = 69°$, 81°, 93°, 117° and 165° covering the maximum of the E2 form factor. Data were taken for 26, 11, 23, 7, and 24 hours, respectively, with an energy resolution of 55 keV. Examples of electron-scattering spectra are shown in Fig. 4.5. The salient peaks correspond to the elastic line, the weakly collective one-phonon 2_1^+ state ($E_x = 0.934$ MeV), the 3_1^- state ($E_x = 2.339$ MeV), and the one-phonon 2_2^+ state ($E_x = 1.847$ MeV) with predominant mixed-symmetry character. The spectra taken in the ^{92}Zr(e,e′) electron scattering reaction were energy calibrated with the previously known excitation energies of the 0_1^+, 2_1^+, 2_2^+ and 3_1^- states [16].

For ^{94}Zr an incident beam energy $E_0 = 71$ MeV with beam currents ranging from 0.5 to 2 μA was used. The ^{94}Zr target has an isotopic enrichment of 96.07% and a thickness of 10 mg/cm^2 [62]. Data were taken at four different scattering angles $\theta = 69°$, 81°, 93° and 165° covering the maximum of the E2 form factor. Data were taken for 10, 14, 29, and 40 hours, respectively, with an average energy resolution of about 60 keV. The measured electron-scattering spectra are shown in Figure. 4.6. The prominent peaks correspond to the elastic line, the weakly collective one-phonon 2_1^+ state ($E_x = 0.918$ MeV), the 3_1^- state ($E_x = 2.057$ MeV), and the one-phonon 2_2^+ state ($E_x = 1.672$ MeV) which is the candidate for the mixed-symmetry state [63]. The spectra taken in the ^{94}Zr(e,e′) electron scattering reaction were energy calibrated with excitation energies of the 0_1^+ , 2_1^+ , 2_2^+ and 3_1^- states given in [64].

In the analysis described in section 8.3 we include data for ^{94}Mo taken from [13]. Data were taken with an incident electron beam energy $E_e =$ 70 MeV and scattering angles 93°, 117°, 141° and 165° with typical beam currents of 2 μA. An 91.6% enriched self-supporting ^{94}Mo target of 9.7 mg/cm^2 areal density was used. In the dispersion-matching mode an energy resolution $E \approx 30$ keV was achieved

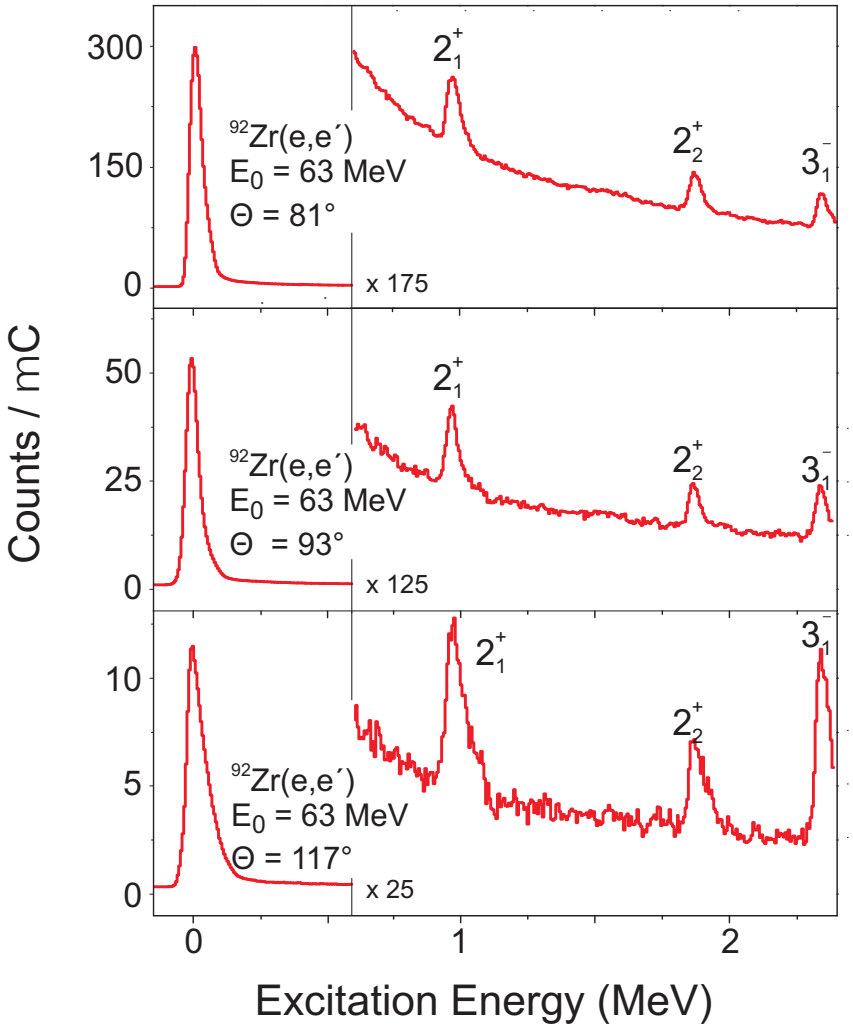

Figure 4.5: Representative electron scattering spectra of the ^{92}Zr(e,e′) reaction at an incident electron energy $E_0 = 63$ MeV and electron scattering angles $\Theta = 81°$, 93° and 117°. Please note the different scale

in this experiment.

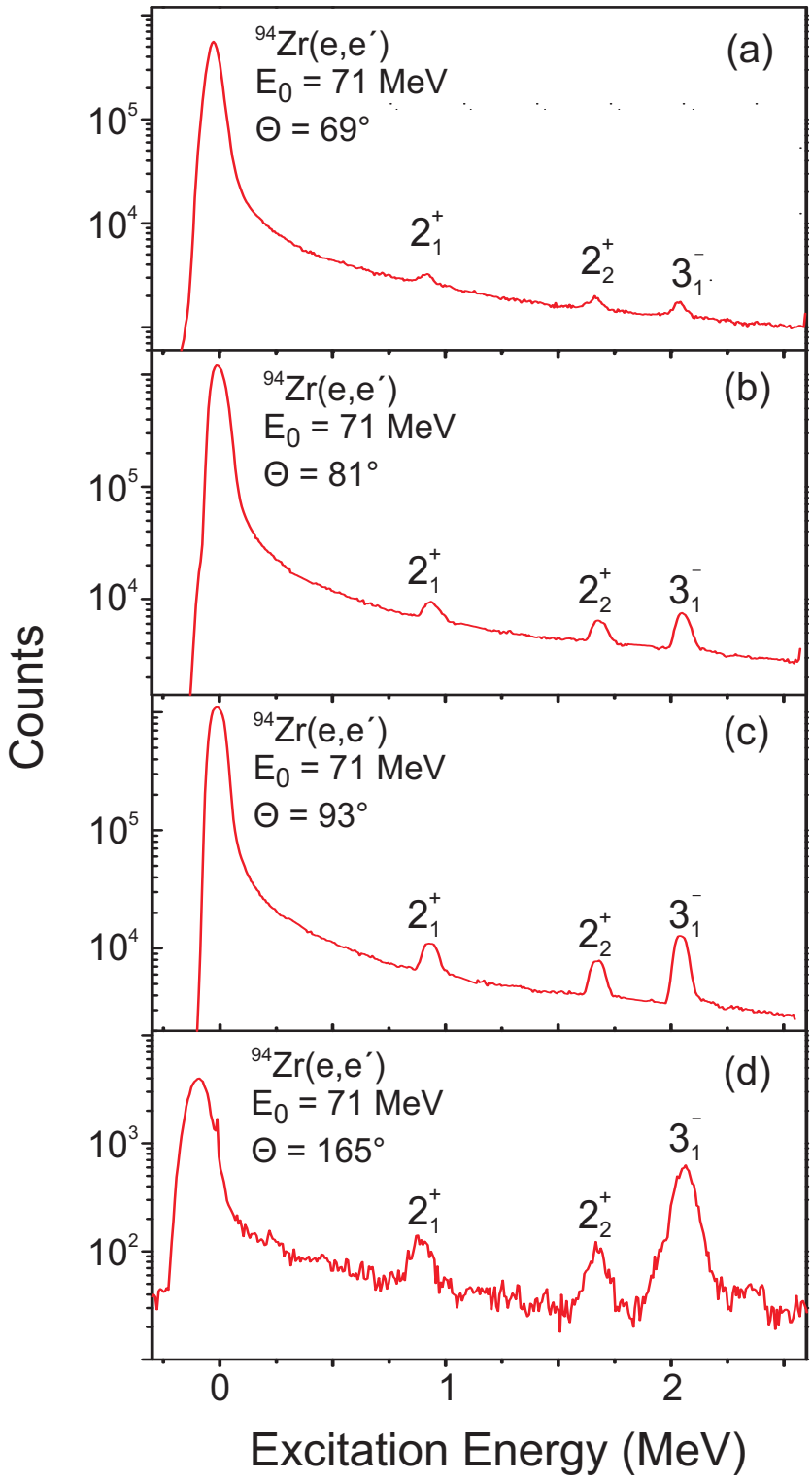

Figure 4.6: Four electron scattering spectra of the ^{94}Zr(e,e′) reaction at incident electron energy $E_0 = 71$ MeV and electron scattering angles $\Theta = 69°$, 81°, 93° and 165°.

5 Data Analysis

5.1 Peak areas and cross sections

The peak areas A_{in}^{exp} of the observed transitions were determined, using the program FIT [65, 66], by assuming an asymmetric Gaussian function for the line shape of the measured spectrum. The $(e, e^{'})$ spectra have a physical background due to radiative processes. For the adjustment of the background, the radiative tail is approximated by a hyperbolic function continuously connected to the Gaussian function. The function is parameterized as

$$y = y_0 \cdot \begin{cases} \exp\left[-\ln 2 \cdot (x - x_0)^2 / \Delta x_1^2\right] & x < x_0 \\ \exp\left[-\ln 2 \cdot (x - x_0)^2 / \Delta x_2^2\right] & x_0 < x \leq x_0 + \eta \Delta x_2 \\ A/(B + x - x_0)^{\gamma} & x > x_0 + \eta \Delta x_2 \end{cases} \tag{5.1}$$

with

x_0	energy,
y_0	count rate at x_0,
$\Delta x_{1,2}$	half width at half maximum for $E_x < x_0$ and $E_x > x_0$, respectively
η	starting point of the radiative tail in units of Δx_2,
γ	exponent of the hyperbolic function of the radiative tail.

The parameters A and B have to fulfill the condition of the continuous differentiable connection of the individual functions at the connection point $x_0 + \eta \Delta x_2$. The area content A_{in}^{exp} is extracted as an integral of the model function (5.1) together with the radiative background approximated as a polynomial using the program FIT [65, 66]. The integration is performed up to a cutoff limit $E_{cutoff} = x_0 + 5\Delta x_1$ and the missing part is considered by multiplying with a radiative correction factor

$$A_{in} = A_{in}^{exp} e^{\delta_s + \delta_B + \delta_I}, \tag{5.2}$$

where δ_s is the Schwinger correction [70]. It takes into account the loss of the peak area due to the loss of electron energy because of the emission of real photons as well as emission and absorption of virtual photons of any energy. δ_B is the Bremsstrahlung correction and accounts for effects which cause an asymmetric distortion of the peak due to small angle scattering from electrons and nuclei other than the initially scattering nucleus [67]. δ_I, the ionization correction (Landau straggling), describes the widening of the peak due to energy loss caused by atomic excitations and ionization. These corrections and their calculations are described in detail in [68–70].

5.2 Energy calibration

The momentum acceptance of the Linttot spectrometer is about 4%. For an initial electron energy of 60 MeV the width of the energy spectrum is about 2.4 MeV. It is sufficient to measure a considerable part of the low-lying excited states but to measure higher excited states one needs to perform several measurements for different settings of the spectrometer magnetic field.
The mean energy loss results from ionization processes caused by the electrons in the target and depends on the effective target thickness d_{eff} and it can be estimated using the expression

$$\Delta E\,[\text{MeV}] = 1.4 \times d_{\text{eff}}\,[\text{g/cm}^2]. \tag{5.3}$$

For measurements at scattering angles $\Theta \leq 141°$ the target was placed in transmission geometry. In this case the effective path length of the electrons is $d_{\text{eff}} = d/\cos(\Theta/2)$ where d_{eff} and Θ are the target thickness and the scattering angle, respectively. In case of $\Theta > 141°$, measurements are possible only in the reflection geometry and the effective path length of the electrons in the target is $d_{\text{eff}} = d/\sin(\Theta/2)$. Taking into account the electron energy loss in the target and assuming a homogeneous magnetic field in the spectrometer, a linear relation holds between the scattered electron energy E' and the channel number N.

$$E'_i = C_1 + C_2 N_i, \tag{5.4}$$

with E_i' and N being the energy of scattered electrons of the i^{th} peak and its corresponding channel number, respectively. The constants C_1 and C_2 are determined by solving a system of linear equations of the type (5.4) for all peaks measured with the same spectrometer magnet field setting

$$E_i' = \frac{(E_i - 0.5\Delta E) - E_x(1 + \frac{E_x}{2Mc^2})}{1 + \frac{2(E_i - 0.5\Delta E)}{Mc^2}\sin^2\frac{\theta}{2}} - 0.5\Delta E, \tag{5.5}$$

where E_i, E_x and M are the initial energy, excitation energy and mass of the target nucleus, respectively. Solving Eq. (5.5) leads to the quadratic equation in E_x. To calibrate the spectra precisely, measurements of transitions with known excitation energies are needed.

5.3 Cross sections

Absolute values of the differential cross sections can be calculated from the corresponding peak areas taking into account the radiative corrections and the dead time of the electronics according to

$$\left(\frac{d\sigma}{d\Omega}\right) = A^{\exp} \cdot \frac{1}{\Delta\Omega} \cdot \frac{e}{It} \cdot \frac{\mu_{\mathrm{mol}}}{d_{\mathrm{eff}} N_A} \tag{5.6}$$

where $\Delta\Omega$ is the spectrometer solid angle [sr], It the accumulated charge of the electron beam incident on the target during the time of the measurement [μC], μ_{mol} the molecular mass, N_A the Avogadro number and $d_{\mathrm{eff}} = \rho\Delta x/\sin(\theta/2)$ in transmission geometry or $d_{\mathrm{eff}} = \rho\Delta x/\cos(\theta/2)$ in the so-called reflection geometry, is the effective areal density of the target and $\rho\Delta x = 9.75$ mg/cm^2 and $\rho\Delta x = 10$ mg/cm^2 the surface density of the ^{92}Zr and ^{94}Zr targets, respectively. In this thesis experimental cross sections for the excited states were extracted by normalization to the cross section of the elastic line because many systematic errors cancel and the achieved precision is higher. Cross sections for elastic electron scattering can be calculated with high precision. Typical systematic uncertainties for the absolute measurement of cross sections at the Linttot spectrometer are presently about 30% neglecting the statistical errors.

5.4 Error estimation

In the present work two analysis methods were used, one is a model independent method and another one is nearly model-independent. In the model-independent-method we need only to determine the peak area and we use the ratios of peak areas that belong to the same spectrum and have the same systematic uncertainties. Thus, all systematic uncertainties are canceled. In the model dependent method inelastic cross sections were calculated relative to the elastic ones which avoids the contribution of systematic uncertainties in the determination of the solid angle and accumulated charge in the Faraday cup as well as the target inhomogeneity. Then, the total uncertainty of measured cross section includes

- statistical uncertainties in the peak area determination from the fit with the model function given by (5.1),
- estimated systematic inaccuracy in the elastic cross section of the order of 5%,

6 One-phonon excitations of ^{92}Zr

The prediction of the IBM-2 with respect to a multi-phonon structure of MSS in vibrational nuclei was confirmed about ten years ago by the observation of large $M1$ transition strengths between low-energy states of ^{94}Mo [9–11]. The 2^+ states were also investigated with electron scattering experiments at the superconducting electron accelerator S-DALINAC and with proton scattering at iThemba LABS [12]. The combined analysis supported a one-phonon structure of the $2^+_{1,3}$ states of ^{94}Mo.

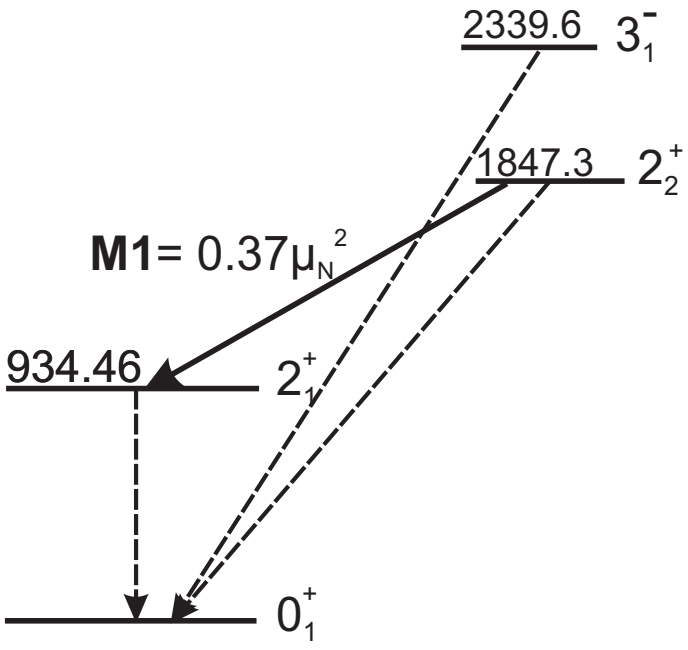

Figure 6.1: The low-lying one-phonon excited states of ^{92}Zr. $M1$ transition strength (solid line) is given in μ^2_N. Dashed lines are presenting the $E2$ and $E3$ transitions.

The neighboring even-even isotone ^{92}Zr with two neutrons outside the $N = 50$ closed shell and with the $Z = 40$ sub-shell closure is the best prototype to investigate the origin of the collective structure toward the double shell closure. In this nucleus a stronger configurational isospin polarization of the one-phonon states than in ^{94}Mo was expected. Indeed, the works of Werner et al. [71] and Holt et al. [14] showed that the picture of good F-spin, in which the 2^+_1 state

approximately has the simple structure $\left|2_1^+\right\rangle \propto |2_\pi^+\rangle + |2_\nu^+\rangle$ and the 2_2^+ the structure $\left|2_{1,ms}^+\right\rangle \propto |2_\pi^+\rangle - |2_\nu^+\rangle$ is too simple. In other words, the F-spin for the 2_1^+ state is strongly broken. The negative experimental value of the g-factor, $g(2_1^+) = -0.18(1)$, suggests an appreciable neutron contribution to the configuration of the 2_1^+ level [72], while the experimental measured positive value of the g-factor $g(2_2^+) = +0.76(50)$ (theoretical value is $+0.9$) indicates a considerable proton contribution to this state [71, 73].
The present section provides an in-depth study of the electron scattering results on ^{92}Zr. Fig. 6.1 shows a part of the level scheme of ^{92}Zr. It displays those levels that are relevant for the discussion in this thesis. The results are interpreted in the framework of the QPM [38].

6.1 Cross sections

Peak areas A of the transitions were obtained from a spectrum decomposition using the line shape described in section 5.1. Absolute differential cross sections

Table 6.1: Cross sections of electroexcitation of the $2_{1,2}^+$ and 3_1^- states in ^{92}Zr normalized to the Mott cross section in units 10^{-4}, $E_0 = 63$ MeV.

θ	q (fm^{-1})	2_1^+	2_2^+	3_1^-
69°	0.36	3.98(23)	2.02(13)	1.95(30)
81°	0.41	5.19(27)	2.67(14)	3.30(13)
93°	0.46	5.39(29)	2.91(17)	4.32(10)
117°	0.55	7.94(45)	4.23(27)	10.5(48)
165°	0.64	5.2(13)	4.4(9)	-

were obtained from normalization to elastic scattering. These are given in Tab. 6.1 normalized to the Mott cross section as a function of the momentum transfer of Eq. (6.1)

$$q_x = \frac{1}{\hbar c}\sqrt{2E_0\,(E_0 - E_x)\,(1 - cos\ \theta) + E_x^2}. \tag{6.1}$$

Besides the statistical uncertainties we have estimated systematical errors of 5%, which were added in quadrature.

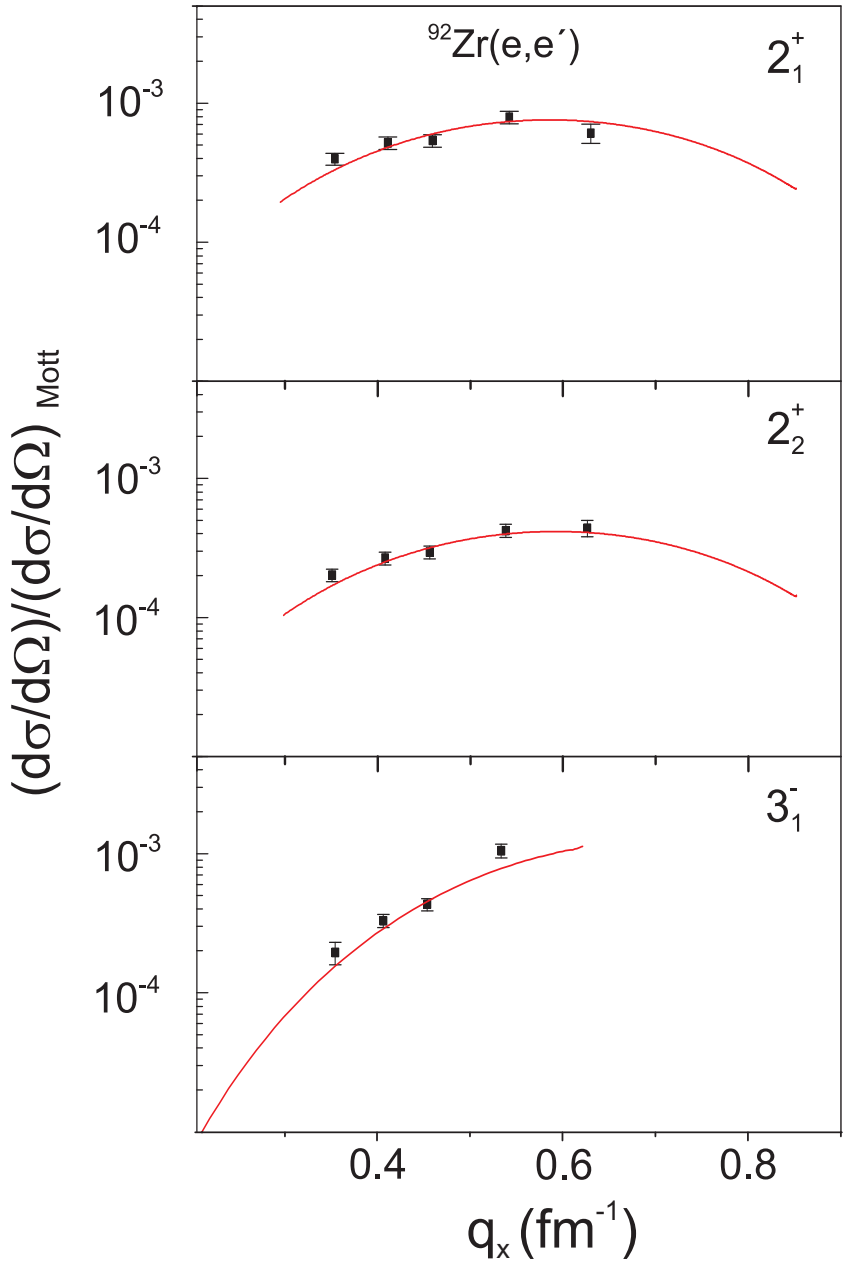

Figure 6.2: Momentum-transfer dependence of the form factor of the one-phonon FS 2_1^+ state (top), MS 2_2^+ state (middle) and 3_1^- state (bottom) of ^{92}Zr from electron scattering. The data (full squares) are compared to the QPM (solid lines).

6.2 Form factors and QPM predictions

The QPM calculations have been performed using the procedure introduced in section 2.4. In the present application excited states of ^{92}Zr are described by wave functions including one-, two-, and three-phonon configurations [74]. In order to fix the coupling parameters $k_{0(1)}^{(\lambda)}$ which determine the strength of the isoscalar (isovector) residual interaction given in the Eq. (2.47)

$$\hat{H}_{\text{r.i.}}^{p-h} = \sum_{\lambda\mu} \sum_{\tau\rho}^{\pm 1} (k_0^{(\lambda)} + \rho k_1^{(\lambda)}) M_{\lambda\mu}^{+}(\tau) M_{\lambda\mu}(\rho\tau),$$

it is required that the excitation energy of the 2_1^+ state and the $B(E2, 2_1^+ \to 0_1^+)$ transition strength are best reproduced. $B(E2)$ and $B(M1)$ transition strengths resulting from this QPM calculation are shown in Tab. 6.2 in comparison with the QPM calculations performed by Lo Iudice and Stoyanov [17] and with the literature experimental data [16]. One sees that there is a satisfactory agreement

Table 6.2: Reduced B($E\lambda$) and B(M1) transition strengths of low-energy collective transitions in ^{92}Zr deduced from the present QPM calculations in comparison with the QPM calculations of Ref. [17] and experimental [16] values. The $B(E2)$ strengths are given in Weisskopf units (W.u.) and the $B(M1)$ strength in μ_{N}^2.

	QPM Present	QPM [17]	Literature [16]	This work DWBA
B($E2; 2_1^+ \to 0_1^+$)	5.9	6.8	6.4(5)	6.18(23)
B($E2; 2_2^+ \to 0_1^+$)	2.6	3.2	3.4(4)	3.31(10)
B($M1; 2_2^+ \to 2_1^+$)	0.64	0.64	0.37(4)	
B($E3; 3_1^- \to 0_1^+$)				18.4(1.1)

between both QPM calculations and the experimental values. The results of the present QPM calculations show a satisfactory agreement with the results of the literature QPM calculations and of the experimental data. We find a strong $M1$ transition between the 2_2^+ and 2_1^+ states that are expected to be the predominant

mixed-symmetry and symmetric states, respectively, of ^{92}Zr and enhanced $E2$ transition strengths for the two states.

Figure 6.2 displays the data from Tab. 6.1 in comparison with the present QPM calculations. Theoretical (e, e') cross sections have been calculated from the QPM wave functions within the Distorted Wave Born Approximation (DWBA) to account for Coulomb distortion effects. The calculations of the cross sections have been performed using the code of Heisenberg and Blok [75] and employing the radial transition charge densities calculated by the QPM. The momentum transfer dependence of the theoretical cross sections is illustrated in Fig. 6.2 as solid lines. Note that the theoretical form factors are absolute values and are not scaled to the experimental data. They provide a satisfactory description of the q dependence as well as of the absolute values. While this is not surprising for the 2^+_1 states because of the calibration of the residual interaction, the good description for the mixed-symmetry 2^+ states is non-trivial.

In order to extract reduced transition probabilities, the calculations have been scaled to the data and extrapolated to the photon point, $q \equiv k = E_x/\hbar c$. The results are given at the right of Tab. 6.2. The absolute $\mathrm{B}(E2; 2^+_1 \rightarrow 0^+_1)$ and $\mathrm{B}(E2; 2^+_2 \rightarrow 0^+_1)$ strengths agree well within error bars with results from previous experiment [16]. This is also true for the $B(E3; 3^-_1 \rightarrow 0^+_1) = 18.4(1.1)$ transition but the present value is significantly more precise. Previous measurements based on low-energy proton scattering show a large spread of results (14.7, 16.2, 18.9, 21.3, 23.6 W.u.) [72], most likely due to the model dependence of the extraction of an electromagnetic transition matrix element from hadronic scattering data.

6.3 Discussion

The (e, e') electron scattering reaction is predominantly a one-step process. Figure 4.5 shows that the 2^+_2 state of ^{92}Zr is almost as strongly populated in (e, e') as the one-phonon 2^+_1 state suggesting a large one-phonon component being present in the wave function of the 2^+_2 state. The similarity of the momentum-transfer dependence of the form factors between the 2^+ states further supports the one-phonon nature of the 2^+_2 state of ^{92}Zr. It is important here to remember that

the theoretical results shown in Fig. 6.2 are absolute and not scaled to the experimental data. The QPM results provide a good description of the (e, e') form factor in this interval of the momentum transfer. As it has been shown in by Walz et al. [18] the wave functions of the one-phonon 2^+ states contains many weak amplitudes of configurations forming the isoscalar Giant Quadrupole Resonance. However their amplitudes are very small. The main configurations of the wave functions are given in Tab 6.3.

Table 6.3: Comparison of main configurations of the $2^+_{1,2}$ states in the present QPM calculations and QPM results of Ref. [17].

	2^+_1		2^+_2	
	Present	[17]	Present	[17]
$\nu\ (2d^2_{5/2})$	0.77	0.57	-0.62	-0.36
$\pi\ (1g^2_{9/2})$	0.37	0.14	0.52	0.39

The QPM calculations predict the main proton and neutron components in the wave functions of the one-phonon 2^+ states to have opposite relative signs which confirms the predominant picture of symmetric and mixed-symmetric character of these states in the valence shell. The 2^+_1 state, because of the large neutron component, is a predominantly symmetric albeit isospin polarized state and the 2^+_2 state is a mixed-symmetric one with a weak isospin polarization. The E2 strengths from the present QPM calculations are close to the values, 6.8 and 3.2 for the 2^+_1 and 2^+_2 state respectively, that were obtained from a QPM calculations performed in Ref. [17]. However, the main components of the wave functions published for the 2^+ states in Ref. [17] show stronger isospin polarization of the 2^+_1 and 2^+_2 states than found in the present calculation. The corresponding results are given in Tab. 6.3.

7 PWBA for heavy nuclei

7.1 Absolute and relative analysis

In the Coulomb field of a large-Z nucleus, the electron waves are significantly distorted. Therefore, the analysis of electron scattering should be performed in the Distorted Wave Born Approximation (DWBA). However, the Plane Wave Born Approximation (PWBA) is much more transparent for the underlying physics mechanisms and provides a clear link between the data and the quantities of interest. Furthermore, the PWBA is a nearly model-independent way to analyze electron scattering data. However, the typical validity limits for PWBA are Z$\leq$ 20 and $E_0 \leq$ 70 MeV [43].

Due to the Coulomb attraction, in the scattering process the effective energy of the electron is larger than its energy in the center-of-mass system. Thus, the momentum transfer increases and shifts the diffraction minima and maxima. The effective momentum transfer is approximately given by [44]

$$q_{\text{eff}} = q \left(1 + \frac{3}{2} \frac{Z\, e^2}{E_i R_{\text{eq}}}\right), \tag{7.1}$$

where R_{eq} is the equivalent radius of a uniformly charged sphere. However, the correction of the experimental form factor to q_{eff} is insufficient for the description of the Coulomb distortion for heavy nuclei. For the electron wave functions, numerically calculated solutions of the Dirac equation by a partial-wave analysis are used. By solving the Dirac equation, the distortion of the electron wave function in the Coulomb field of the nucleus is taken into account. This is called Distorted Wave Born Approximation (DWBA). The DWBA form factor was already defined in Eq. (3.1).

In comparison to PWBA this quantity is not only a function of the momentum transfer, but also depends explicitly on the initial electron energy E_i and scattering angle θ. After calculating the cross section in DWBA, a correction factor can be defined as

$$f_{\text{C}} = \frac{(d\sigma/d\Omega)_{DWBA}}{(d\sigma/d\Omega)_{PWBA}}, \tag{7.2}$$

which allows the representation and interpretation of the form factor as a function of the momentum transfer in analogy to PWBA.

In light nuclei it has been shown that transition strengths can be extracted in a nearly model-independent PWBA analysis [43]. It assumes that Coulomb distortions of the electron wave function can be approximated by an overall correction factor determined from the g.s. charge distribution of the nucleus. The differential cross sections in the PWBA for nuclear excitation can be written as a sum over the cross section for electric and magnetic multipole transitions that can be converted to the DWBA cross section using Coulomb correction factors

$$\begin{aligned}\left(\frac{d\sigma}{d\Omega}\right)_{E\lambda} =& f_{\mathrm{C}}\left(\frac{d\sigma}{d\Omega}\right)_{E\lambda,PWBA} = f_{\mathrm{C}}\frac{\alpha^2 a_\lambda q_{\mathrm{x}}^{2\lambda}}{k_0^2 R} \\ & \left(\frac{\lambda}{\lambda+1}V_L(\theta)B(C\lambda,q_{\mathrm{x}}) + V_T(\theta)B(E\lambda,q_{\mathrm{x}})\right),\end{aligned} \tag{7.3}$$

$$\left(\frac{d\sigma}{d\Omega}\right)_{M\lambda} = f_{\mathrm{C}}\left(\frac{d\sigma}{d\Omega}\right)_{M\lambda,PWBA} = f_{\mathrm{C}}\frac{\alpha^2 a_\lambda q_{\mathrm{x}}^{2\lambda}}{k_0^2 R}V_T(\theta)B(M\lambda,q), \tag{7.4}$$

where
$a_\lambda = 4\pi\lambda^{-1}\left(\lambda+1\right)\left[(2\lambda+1)!!\right]^{-2}$,
$k_0 = E_0/\hbar c$, and
$R = 1 + \hbar c(k_0/Mc^2)(1-\cos\theta)$.
The symbol α denotes the fine structure constant.
With Siegert's theorem $B(E\lambda,q_{\mathrm{x}}) = k^2/q^2 B(C\lambda,q_{\mathrm{x}})$ connecting $B(C\lambda)$ and $B(E\lambda)$, the reduced transition probabilities in PWBA can be related to the experimental differential cross section by

$$\begin{aligned}B(C\lambda,q_{\mathrm{x}}) &= \frac{k_0^2 R}{\alpha^2 a_\lambda q_{\mathrm{x}}^{2\lambda}}\frac{1}{\left[V_L(\theta)\left(\frac{\lambda}{\lambda+1}+\frac{k_{\mathrm{x}}^2}{q_{\mathrm{x}}^2}\frac{V_T(\theta)}{V_L(\theta)}\right)f_{\mathrm{C}}\left(q_{\mathrm{x}},E_0,E_x\right)\right]}\left(\frac{d\sigma}{d\Omega}\right)_{E\lambda} \\ &= \frac{1}{\left[f_{\mathrm{kin}}f_{\mathrm{C}}\left(q_{\mathrm{x}},E_0,E_x\right)\right]}\left(\frac{d\sigma}{d\Omega}\right)_{E\lambda}\end{aligned} \tag{7.5}$$

For low momentum transfers, $B(C\lambda,q_{\mathrm{x}})$ can be expanded in a power series of the q_{x}^2

$$\sqrt{B(C\lambda,q_{\mathrm{x}})} = \sqrt{B\left(C\lambda,0\right)}\left(1-\frac{q_{\mathrm{x}}^2}{2\left(2\lambda+3\right)}R_{\mathrm{tr}}^2+\frac{q_{\mathrm{x}}^4}{8\left(2\lambda+3\right)\left(2\lambda+5\right)}R_{\mathrm{tr}}^4-\cdots\right) \tag{7.6}$$

In order to relate $B(C\lambda,q_{\mathrm{x}})$ to the γ-ray reduced transition probability $B(E\lambda,k)$ we the Siegert theorem $B(C\lambda,0) = B(E\lambda,0)$ and assume $B(E\lambda,0)\approx B(E\lambda,k)$.

Here, the transition radius $R_{\rm tr}$ is defined by

$$R^n_{\rm tr} = \frac{\langle r^{n+\lambda}\rangle_{\rm tr}}{\langle r^{\lambda}\rangle_{\rm tr}} = \frac{\int \rho^{\lambda}_{\rm tr} r^{n+^{\lambda}} d^3r}{\int \rho^{\lambda}_{\rm tr} r^{^{\lambda}} d^3r} \tag{7.7}$$

where $\rho^{\lambda}_{\rm tr}(r)$ is the transition density of multipolarity λ. One can then write for the ratio of the transition strengths of the $2^+_{1,2}$ states:

$$\sqrt{\frac{B(C2,q_2)}{B(C2,q_1)}} \approx \sqrt{\frac{B(E2,k_2)}{B(E2,k_1)}} \left(\frac{1 - \frac{q_2^2}{14}\left(R_{\rm tr,2}\right)^2 - \frac{q_2^4}{504}\left(R_{\rm tr,2}\right)^4}{1 - \frac{q_1^2}{14}R^2_{\rm tr,1} - \frac{q_1^4}{504}R^4_{\rm tr,1}} \right). \tag{7.8}$$

The quantity $\Delta R_{\rm tr} = R_{\rm tr,2} - R_{\rm tr,1}$ is the difference of the corresponding charge-transition radii. Here $q_{1,2}$ denotes $q_{\rm x}$ from Eq. (3.4) with $E_{\rm x} = E_{1,2}$ and is written as a function of elastic momentum transfer q. With that we obtain

$$\sqrt{\frac{B(C2,q_2)}{B(C2,q_1)}} \approx \sqrt{\frac{B(E2,k_2)}{B(E2,k_1)}} \left(\frac{1 - \frac{q_2^2}{14}\left(R_{\rm tr,1} + \Delta R\right)^2 - \frac{q_2^4}{504}\left(R_{\rm tr,1} + \Delta R\right)^4}{1 - \frac{q_1^2}{14}R^2_{\rm tr,1} - \frac{q_1^4}{504}R^4_{\rm tr,1}} \right). \tag{7.9}$$

The quantity $B(E2,k_2)/B(E2,k_1)$ is the ratio of the $B(E2)$ strengths to the second and first 2^+ states. In Eq. (7.9) the assumption $R^4_{\rm tr,1} = (R^2_{\rm tr,1})^2$ has been used which is not obvious considering the definition Eq. (7.7). Its justification and other aproximations are discussed in the following section.
Employing Eqs. (3.4), (5.6), (7.5) and (7.6), the ratio of reduced transition strengths can be approximated by

$$\sqrt{\frac{B(C2,q_2)}{B(C2,q_1)}} = \sqrt{\frac{\left[f_{\rm kin} f_{\rm C}\left(q_1, E_0, E_{x1}\right)\right]\left(\frac{d\sigma}{d\Omega}\right)_{E\lambda,2^+_2}}{\left[f_{\rm kin} f_{\rm C}\left(q_2, E_0, E_{x2}\right)\right]\left(\frac{d\sigma}{d\Omega}\right)_{E\lambda,2^+_1}}} = R_{\rm F}(q)\sqrt{\frac{A_2}{A_1}} \tag{7.10}$$

with

$$R_{\rm F}(q) = \sqrt{\frac{\left[f_{\rm kin} f_{\rm C}\left(q_1, E_0, E_{x1}\right)\right]}{\left[f_{\rm kin} f_{\rm C}\left(q_2, E_0, E_{x2}\right)\right]}} \tag{7.11}$$

and finally by combining Eqs.(7.9) and (7.10)

$$R_{\mathrm{F}}(q)\sqrt{\frac{A_2}{A_1}} \approx \sqrt{\frac{B(E2,k_2)}{B(E2,k_1)}} \left(\frac{1-\frac{q_2^2}{14}\left(R_{\mathrm{tr},1}+\Delta R\right)^2 - \frac{q_2^4}{504}\left(R_{\mathrm{tr},1}+\Delta R\right)^4}{1-\frac{q_1^2}{14}R_{\mathrm{tr},1}^2 - \frac{q_1^4}{504}R_{\mathrm{tr},1}^4} \right), \tag{7.12}$$

where the indices $1, 2$ indicate the transitions to the 2_1^+ and 2_2^+ state, respectively. R_F denotes the ratio of kinematic functions $\sqrt{f_{kin,2}/f_{kin,1}}$. The experimental ratio depends on the square root of the ratio of the peak areas $\sqrt{A_2/A_1}$ only.

7.2 Tassie Model

The Tassie model is a hydrodynamical model applicable for non-uniform nuclear charge and mass density distributions. Excited states are described as oscillations of the shape of the nucleus. They are deviations from the spherical symmetry of the mass and charge distributions of the nucleus with radius r_0 [76]. The model should thus provide a good approximation for collective transitions in vibrational nuclei. The following discussion is restricted to charge densities $\rho_0(r)$ of spherical symmetry. No deformation effects are considered. It is assumed that in treating low-lying nuclear energy levels, the radial dependence of the density distributions does not change appreciably.
For the excited states we assumed that under distortion, the element of the charge distribution changes without any alteration of the volume, i.e.

$$\rho(\mathbf{r}) = \rho_0(r_0), \tag{7.13}$$

which means that each element of mass and charge is incompressible. The shape of the distortion, which is the difference between the charge density distributions of the ground and the excited states, is then given by [76]

$$r - r_0 = \sum_{l=2,\ m} \alpha_{lm}(r_0) Y_{lm}(\Theta,\varphi) r_0^{l-1} \tag{7.14}$$

where Y_{lm} is the spherical harmonic.
In the Tassie model the transition densities are given by [76]

$$\begin{aligned} \delta\rho_\lambda(r) &= r^{\lambda-1}\frac{d\rho_0(r)}{dr} \\ \rho_0(r) &= \frac{\rho_0}{1+\exp[\alpha(r-r_0)]} \end{aligned} \tag{7.15}$$

i.e., $\rho_0(r)$ has the form of the Woods-Saxon mean field and $R_0 = r_0 A^{1/3}$ is the nuclear radius.
In the following we use the Tassie model to study the effect of the Coulomb corrections on the extraction of the transition radius difference and on the extrapolated value of the ratio of the B(E2) strengths using Eq. (7.12). Another important question is the sufficient number of q^{2n} terms of the expransion (7.6) to be included in Eq. (7.12) in order to get the best result in the region of experimentally covered momentum transfer. Finally it is investigated to what extent R^4_{tr} and R^6_{tr} can be approximated by $(\mathrm{R}^2_{tr})^2$ and $(\mathrm{R}^2_{tr})^3$, respectively.
The analysis is performed for the case of ^{92}Zr but the results are also representative for the other nuclei studied.

7.2.1 Model parameters

In order to stay close to the experimental conditions we have adjusted α, r_0, and ρ_0 parameters in (7.15) so that the transition density of the Tassie Model reproduces the surface behavior of $\delta\rho_\lambda(r)$ for the 2^+_1 state of ^{92}Zr calculated within the QPM. However, for the 2^+_2 state we have arbitrarily reduced the value of r_0, which allows us to subsequently test how accurate our method is in the case of a large difference of the transition radii for the two states. The corresponding transition densities are plotted in Fig (7.1). The dotted and dashed lines are the transition density of the 2^+_1 and the 2^+_2 states with the parameters $\alpha = 1.85$ fm^{-1}, $\rho_0 = 4.9 \cdot 10^{-3}$ e^{2}fm^{-3} and $r_0 = 0.965$ fm^{-1} (2^+_1) and $r_0 = 0.800$ fm^{-1} (2^+_2) respectively.

7.2.2 DWBA analysis of the charge transition densities

In this section we extracted the corresponding form factors within a DWBA approach that can then be used in our experimental conditions. A set of (E_x, q)

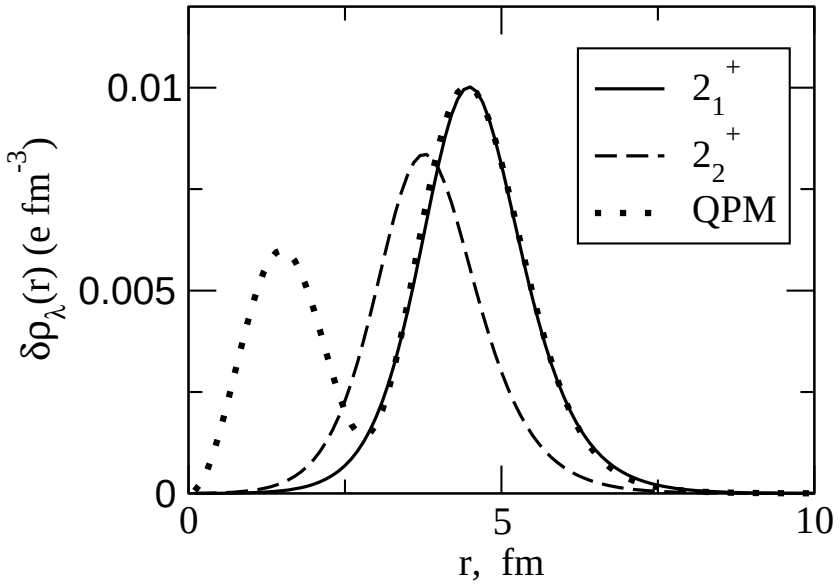

Figure 7.1: Radial charge transition density distribution of the excitation of the 2_1^+ state in ^{92}Zr from QPM calculations (dotted line). The solid line is the charge transition density of the 2_1^+ in the Tassie model adjusted to the QPM. The dashed line is the charge transition density of the 2_2^+ assumed in the Tassie model.

values covering the typical energy and momentum transfer range of the data discussed in the following section is given in Tab. 7.1.

Table 7.1: Scattering angles and corresponding momentum transfers for typical excitation energies of the 2_1^+ and 2_1^+ states and the elastic momentum transfers.

	($E_x = 0.0$ MeV)	($E_x = 1.0$ MeV)	($E_x = 2.5$ MeV)
Θ	q^2 (fm^{-2})	$q^2_{2_1^+}$ (fm^{-2})	$q^2_{2_2^+}$ (fm^{-2})
60^o	0.1258	0.1241	0.1215
85^o	0.2297	0.2265	0.2217
110^o	0.3377	0.3329	0.3258
135^o	0.4296	0.4235	0.4144
160^o	0.4881	0.4812	0.4709

The calculated form factors $|F(q^2)|^2 = (d\sigma/d\Omega)/(d\sigma/d\Omega)_{\rm Mott}$(top) and their ratios (bottom) are presented in Fig. 7.2. Furthermore we have calculated the rel-

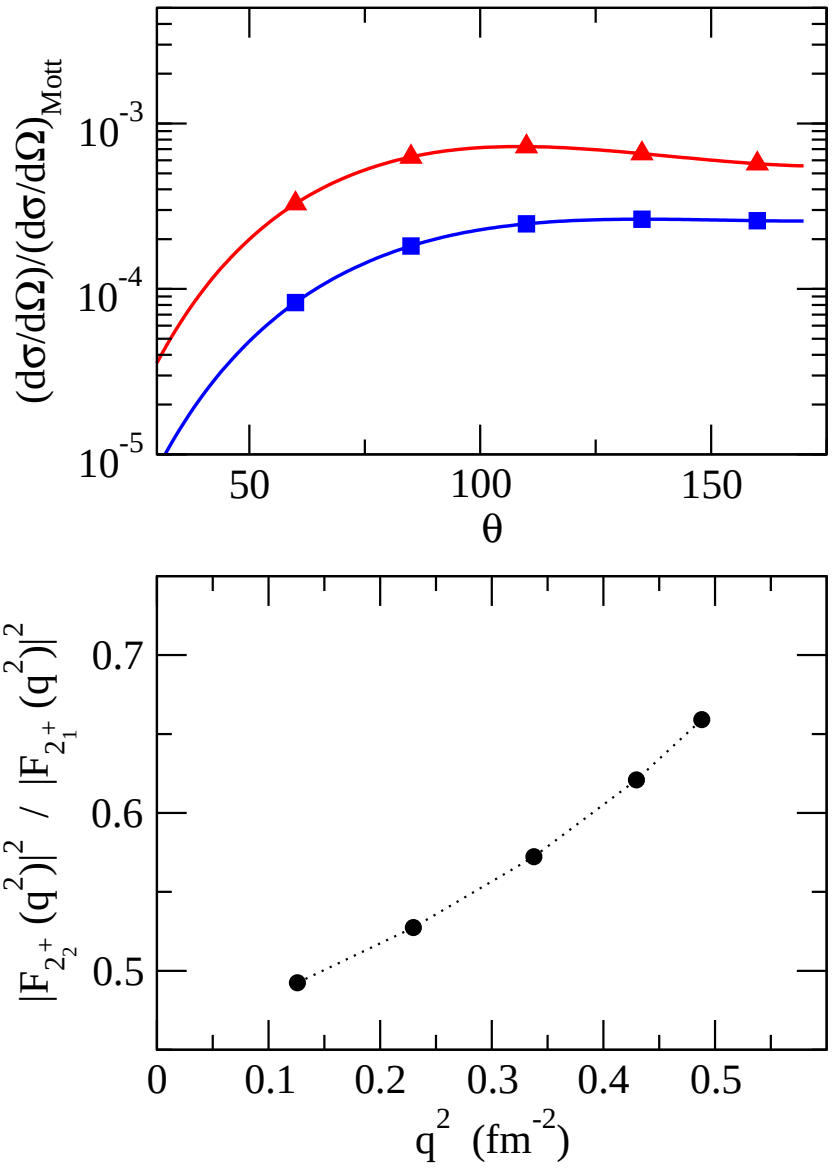

Figure 7.2: (top) Momentum transfer dependence of the form factors of 2_1^+ (line with triangles) and the 2_2^+ (line with squares) states. (bottom) Momentum transfer dependence of their ratio.

ative quantities to test Eq. (7.12) from the transition densities shown in Fig. 7.1. The $B(E2)$ strengths, transition radii for the 2_1^+ and the 2_2^+ states, and the second and forth momenta of the charge transition radii are summarized in Table 7.2.

The ratio of the $B(E2)$ strengths in this case is $B(E2, gs \rightarrow 2_2^+)$ / $B(E2, gs \rightarrow 2_1^+) = 0.2158$ and the transition radius difference obtained from this calculations is $\Delta R = -0.55$ fm.

Table 7.2: The calculated $B(E2)$ strengths and the transition radii for the 2_1^+ and the 2_2^+ states and the second and forth momenta of the charge transition radius

	$E_{\rm x}$	r_0	$B(E2)$	$R_{\rm tr}^2$	$R_{\rm tr}^4$
0^+		0.0			
2_1^+	1.0	0.965	719.6	30.218	1081.321
2_2^+	2.5	0.800	155.3	24.473	746.259

7.2.3 PWBA analysis of the charge transition densities

In order to test our model-independent analysis for the electron scattering data, we have used Eq.(7.12) to calculate the momentum transfer dependence of the ratio of the reduced transition probabilities for the fixed value of the transition radius of the 2_1^+ state ($R_{tr,1}$) and five different values of the transition radius difference ($\Delta R = -0.08$, -0.38, -0.55, -0.73, -1.04) fm. The obtained curves were normalized to the ratio given in Tassie calculations (doted line in Fig. 7.3) at the lowest momentum transfer $q = 0.1258$ fm^{-2}

$$\sqrt{\frac{B(C2,q_2)}{B(C2,q_1)}} \approx \sqrt{\frac{B(E2,k_2)}{B(E2,k_1)}}\sqrt{\frac{f_c(2_2^+)}{f_c(2_1^+)}}\left(\frac{1-\frac{q_2^2}{14}\left(R_{\rm tr,1}+\Delta R\right)^2-\frac{q_2^4}{504}\left(R_{\rm tr,1}+\Delta R\right)^4}{1-\frac{q_1^2}{14}R_{\rm tr,1}^2-\frac{q_1^4}{504}R_{\rm tr,1}^4}\right),$$

The corresponding curves in Fig. 7.3 for the different ΔR values show a significant sensitivity to the transition radii difference. For $\Delta R = -0.55$ fm there is a very good agreement between the DWBA and the model-independent analysis. Furthermore, the extracted ratio of the E2 excitation strengths at the same $\Delta R = -0.55$ fm equals 0.2147, i.e. it deviates only about 0.5% from the value obtained from integrating the Tassie transition densities. This means that we were able to reproduce the ratios of the DWBA results within the PWBA with

good accuracy. Figure 7.3 also shows that the ratio of the $B(E2)$ values does not change dramatically when the transition radii difference changes. These calculated ratios of the form factors are normalized to the model data at very low momentum transfer, where the Coulomb corrections ratio approaches one.

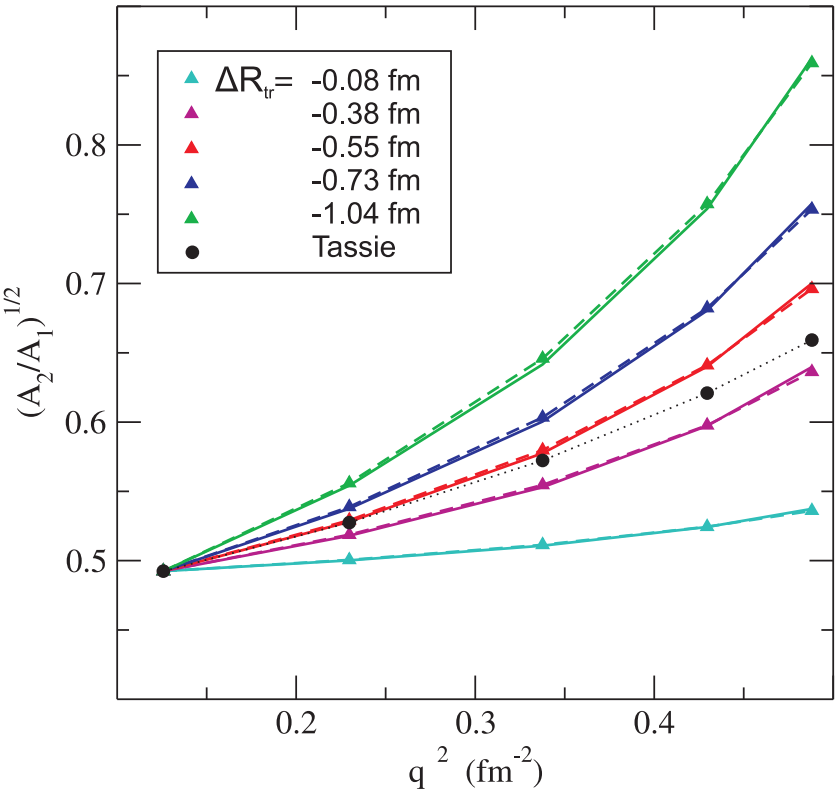

Figure 7.3: Ratio of the form factors as a function of the squared momentum transfer for a given B(E2) ratio and five different transition radii differences using Eq.(7.12) in comparison to that extracted from the DWBA analysis (Solid lines) for the assumption that $R^4_{\mathrm{tr},1} = (R^2_{\mathrm{tr},1})^2$ (Dashed lines) for calculated values of $R^2_{\mathrm{tr},1} R^4_{\mathrm{tr},1}$

Another important question is whether the ratio of the Coulomb corrections of the two states depends on the transition radii difference. We have taken five different values of the squared momentum transfer given in Fig. 7.4 and for each value calculated the ratio of Coulomb corrections $f_c(2^+_2)/f_c(2^+_1)$ for transition radii differences $\Delta R = 0 \; - \; 2$fm.

Figure 7.4 shows that the ratio of the Coulomb correction change solely slightly

for small transition radii difference as expected for ^{92}Zr but for large transition radii differences this ratio can change appreciably. That means that the Coulomb corrections do not cancel and have to be included explicitly in the analysis if a considerable transition radii difference is expected.

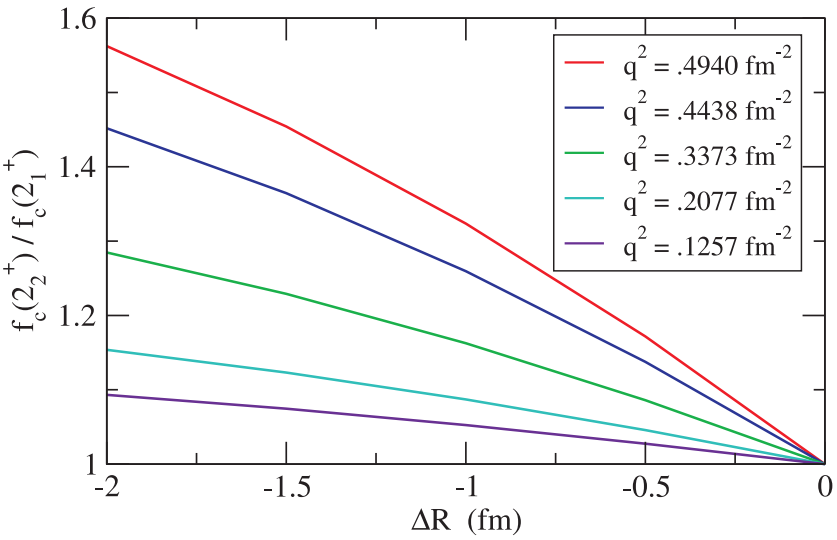

Figure 7.4: Dependence of the ratio of the Coulomb corrections on the transition radii difference.

In the Eq. (7.12) the assumption $R^4_{\mathrm{tr},1} = (R^2_{\mathrm{tr},1})^2$ have been used. The employment of $R^4_{\mathrm{tr},1}$ instead of $(R^2_{\mathrm{tr},1})^2$ in the Eq. (7.12) exhibits no substantial deviations, as shown by the dashed lines in Fig. (7.3).

8 B(E2) strengths and the transition radii difference

Here, we discuss the application of the new method for a model-independent determination of the ratio of the $E2$ transition strengths and the transition radii difference of fully symmetric and mixed-symmetric one-phonon excitations in heavy vibrational nuclei presented in the previous section.

8.1 ^{92}Zr

As shown in Eq. (7.12), the ratio of the B(E2) strengths and the transition radii difference between the 2_1^+ and 2_2^+ states depends only on the peak areas calculated from the measured electron scattering spectra. The measured peak areas and the ratio of the kinematical functions $R_F(q)$ defined in Eq. (7.11) are given in Table 8.1.

Table 8.1: Peak areas of electroexcitation of the $2_{1,2}^+$ states in ^{92}Zr and the ratio R_F of the $2_{1,2}^+$ kinematical functions defined in Eq. (7.11).

Θ	q^2 (fm^{-2})	2_1^+	2_2^+	R_F
69°	0.127	15692(518)	8161(395)	1.0148
81°	0.171	92140(925)	46317(565)	1.0146
93°	0.214	11587(252)	6055(186)	1.0146
117°	0.299	1688(70)	851(59)	1.0143

Figure 8.1 shows the Coulomb-correction factors calculated with the QPM for the transitions to 2_1^+ (middle) and 2_2^+ (top) states in ^{92}Zr together with their ratio (bottom) as a function of q. The ratio is unity to better than 1 % over the range of the momentum transfer included in our experiments. Consequently, the effects from Coulomb distortion can be neglected in a relative analysis, and the extraction of the $B(E2)$ ratio can be achieved with improved accuracy, since sys-

tematic errors in the determination of absolute cross sections cancel each other. Figure 8.2 shows a plot of $R_{\rm F}\sqrt{A_2/A_1}$ as a function of the squared elastic mo-

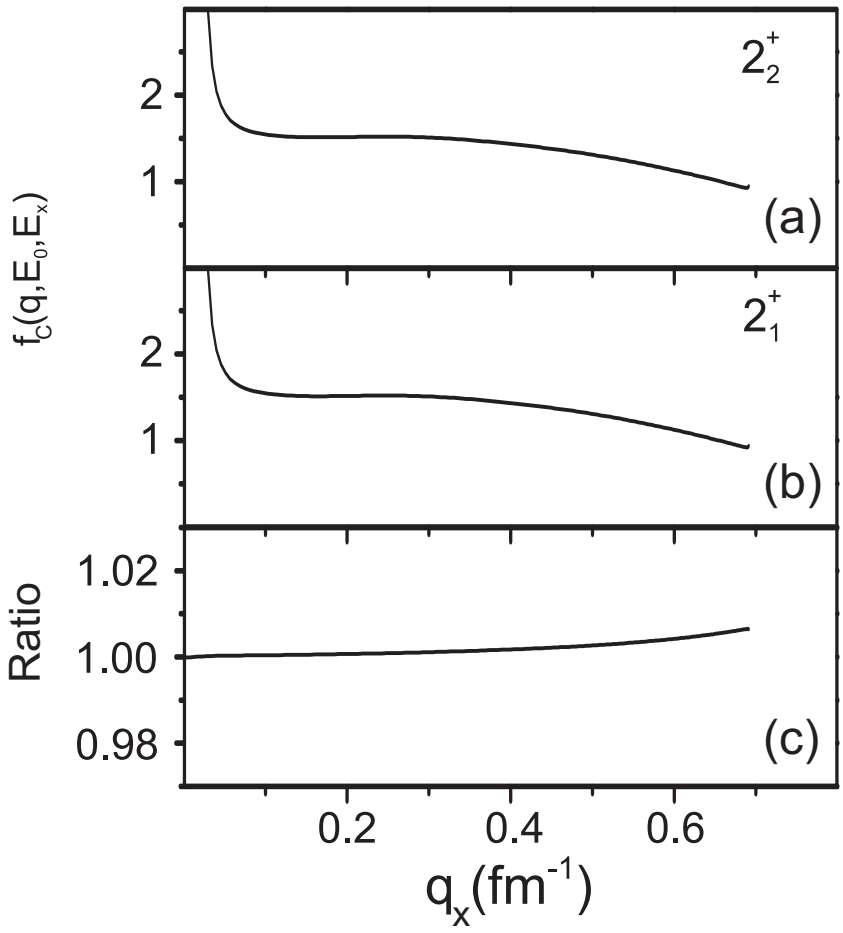

Figure 8.1: Momentum-transfer dependence of the Coulomb corrections for the transition to the $2^+_{1,2}$ states in ^{92}Zr for an incident electron energy $E_0 = 63$ MeV.

mentum transfer. A fit of Eq. (7.12) to the data has 3 parameters, viz. the ratio of $B(E2)$ strengths, $R_{\rm tr,1}$ and ΔR. In a first step, $R_{\rm tr,1} = 5.6$ fm is fixed using the QPM results. A χ^2-minimization of Eq.(7.12) to the data then determines $\sqrt{B(E2;2^+_2)/B(E2;2^+_1)} = 0.720(8)$. With the $B(E2;2^+_1)$ value from Tab. 6.2, we obtain $B(E2;2^+_2) = 3.32(27)$ W.u.. The second parameter ΔR in Eq. (7.12) is a measure of the change of the proton transition radii between both 2^+ states. The fit of Eq. (7.12) leads to $\Delta R = -0.18(65)$ fm, where the uncertainty is dominated by the limited number of data points.

One way to improve the fit is the inclusion of the results of Ref. [16] providing

an additional data point at $q_0 = k$. The resulting fit (solid curve) with 1σ error bars (dashed curves) shown in Fig. 8.2 leads to $\Delta R = -0.12(51)$ fm consistent with equal proton transition radii.

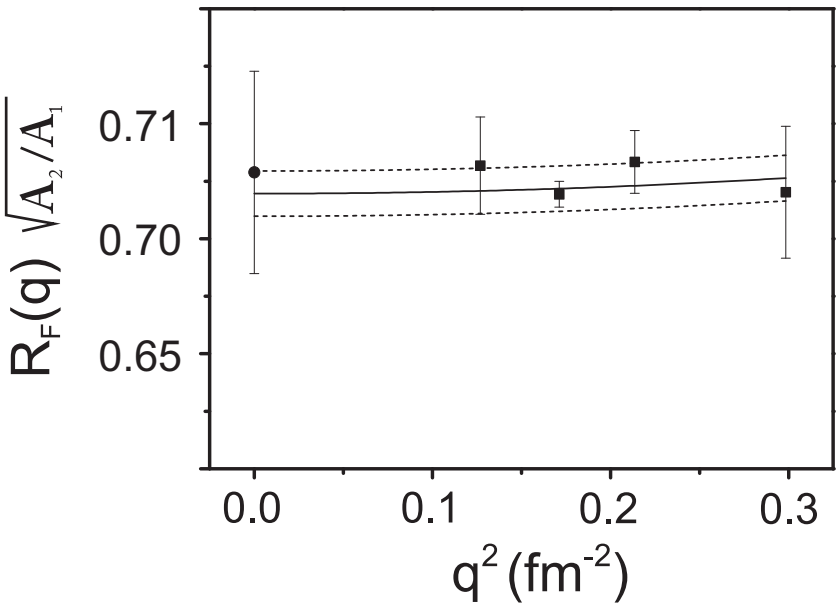

Figure 8.2: Ratio of the reduced transition probabilities of the 2^+ MSS and FSS (solid squares) of ^{92}Zr as a function of the squared elastic momentum transfer q_0. An additional data point (full circle) at $q_0^2 = k^2$ stems from the ratio of $B(E2)$ strengths obtained from γ-decay lifetime measurements [16]. The solid line is a fit of Eq. (7.12) with 1σ error bars given by the dashed lines.

In order to discuss a possible dependence of the result on a variation of the absolute size of the charge transition radius $R_{\mathrm{tr},1}$ [42], we have repeated the analysis for 9 different values of $R_{\mathrm{tr},1}$ between 4.6 and 6.7 fm, thereby overexhausting the range of possible values expected from model calculations and from the phenomenological finding that the transition radii of collective excitations differ not too much from the radius of the nuclear ground state [43]. As demonstrated in Fig. 8.3, the deduced difference of the charge transition radii is independent of the choice of $R_{\mathrm{tr},1}$. This is particular interesting in view of the recent results of Walz *et al.* [18] providing evidence for a significant difference of the neutron transition

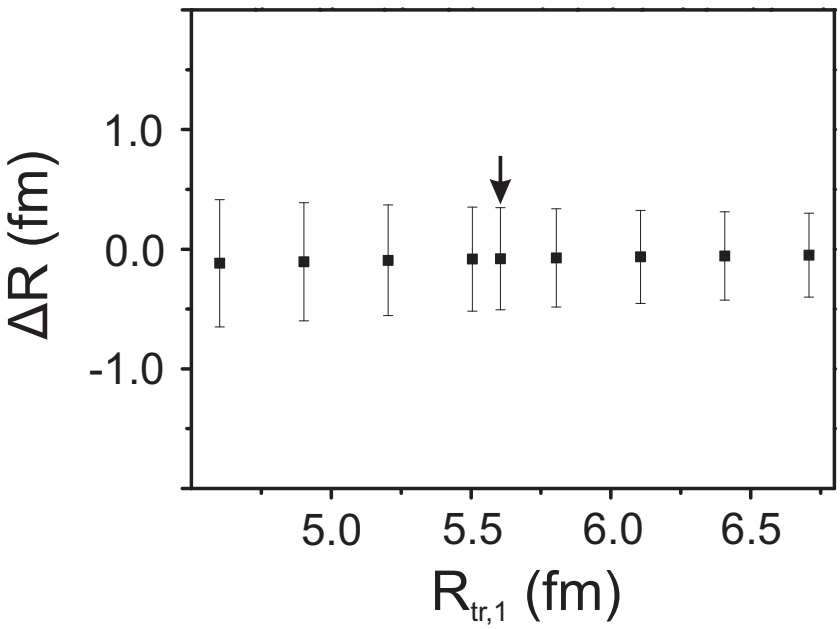

Figure 8.3: Evolution of the charge-transition radii difference between the 2_1^+ and 2_2^+ states in ^{92}Zr obtained from Eq. (7.12) as a function of the transition radius $R_{\mathrm{tr},1}$. the arrow indicates the prediction of the QPM calculation.

radii for these two states, while their proton transition radii are expected to be very close based on QPM calculations. This may serve as a new experimental signature of MSS in vibrational nuclei with a specific shell structure. The present results fully confirm this conclusion.

The ratio of $B(E2, 2^+)$ values are in agreement with Ref. [16] and with the value obtained above from the DWBA analysis. While the ratio can be determined precisely with an uncertainty of about 1%, the accuracy of the absolute value is presently limited by the error of the $B(E2; 2_1^+)$ value in the literature.

8.2 ^{94}Zr

^{94}Zr has four neutrons beyond the N = 50 closed shell and 40 protons. Table 8.2 shows the measured peak areas of the $2_{1,2}^+$ in ^{94}Zr deduced from the $(e, e^{'})$ experiment described in section 4 and the ratio of the kinematical functions $R_F(q)$

defined in Eq. (7.11).

Table 8.2: Peak areas of electroexcitation of the $2^+_{1,2}$ states in ^{94}Zr in units of counts and the ratio R_F of the $2^+_{1,2}$ kinematical functions defined in Eq. (7.11).

Θ	q^2 (fm^{-2})	2^+_1	2^+_2	R_F
69°	0.166	4796(271)	4455(839)	1.0106
81°	0.218	27431(394)	21981(394)	1.0106
93°	0.273	55823(458)	43789(367)	1.0106
165°	0.509	852(49)	785(40)	1.0064

Figure 8.4 shows a plot of $R_{\rm F}\sqrt{A_2/A_1}$ as a function of the squared elastic momentum transfer.

In the fit of Eq. (7.12) to the data we have fixed the $R_{\rm tr,1}$ to the same value as for ^{92}Zr, $R_{\rm tr,1} = 5.6$ fm. In this case we only have two parameters, the ratio of $B(E2)$ strengths and ΔR. A χ^2-minimization of Eq.(7.12) to the data then determines $B(E2;2^+_2)/B(E2;2^+_1) = 0.823(46)$ in contradiction to the result from Ref. [64] ($B(E2;2^+_2)/B(E2;2^+_1) = 1.63(37)$) but in a very good agreement with Ref. [63], who find $B(E2;2^+_2)/B(E2;2^+_1) = 0.79(10)$. With the value $B(E2;2^+_1) = 4.9(11)$ W.u. from Ref [63], we obtain using our result $B(E2;2^+_2) = 4.0(13)$ W.u.. This demonstrates again that a PWBA analysis of the electron scattering data is a very good tool, which can be applied for heavy nuclei, to extract the ratio of the g.s. $B(E2)$ transition strengths precisely in a relative analysis.
We can find that the mixed-symmetric 2^+_2 in ^{94}Zr still has relative weakly $E2$ transition in agreement with the known signature for symmetry and mixed symmetric one phonon excitations. Concerning the transition radii difference, the fit of Eq. (7.12) leads to $\Delta R = -0.24(34)$ fm, where the uncertainty here is dominated by the energy resolution of the electrons beam and the limited number of data points. Again the value is compatible with 0.
The combined analysis of (p,p') and (e,e') will provide test of the applicability of the conclusion [18]. The sign change of the leading proton and neutron component between FSS and MSS can be measured by comparison of proton and

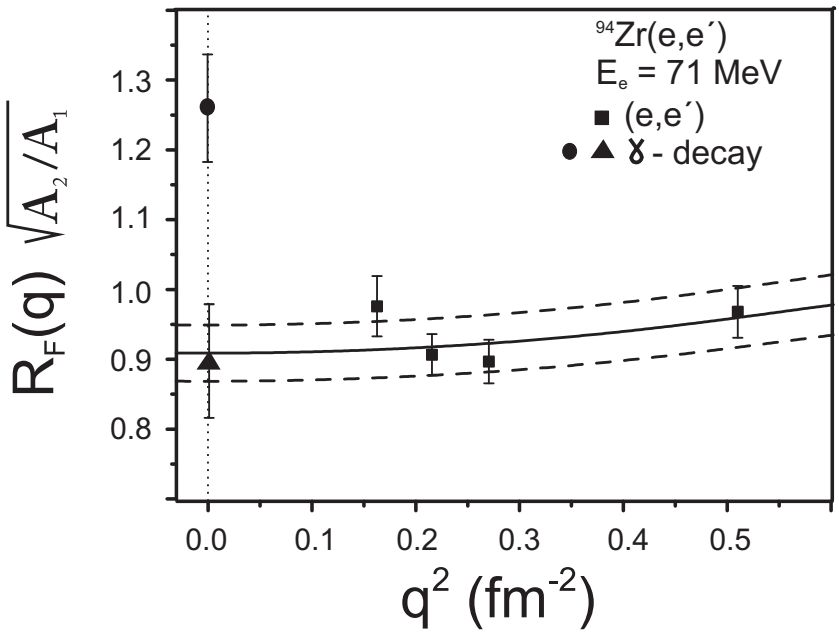

Figure 8.4: Ratio of the reduced transition probabilities of the 2^+ MSS and FSS (solid squares) of ^{94}Zr as a function of the squared elastic momentum transfer q_0. An additional data point (full circle) at $q_0^2 = k^2$ stems from the ratio of $B(E2)$ strengths obtained from γ-decay lifetime measurements [64]. The solid line is a fit of Eq. (7.12) with 1σ error bars given by the dashed lines.

neutron transition radii.

In order to examine the dependence of the result on a variation of the absolute size of the charge transition radius $R_{\mathrm{tr},1}$. We have repeated the analysis described for ^{92}Zr, Fig. 8.5 shows that the extracted ΔR is independent of the choice of $R_{\mathrm{tr},1}$.

8.3 ^{94}Mo

^{94}Mo is formed by Z = 42 protons with two protons out of the subshell-closure and N = 50 with two neutron out of the shell-closue. The picture of multi-phonon structure of MSS in vibrational nuclei was fully confirmed in ^{94}Mo [11]. In this section we apply the new PWBA relative analysis on the electron scattering data

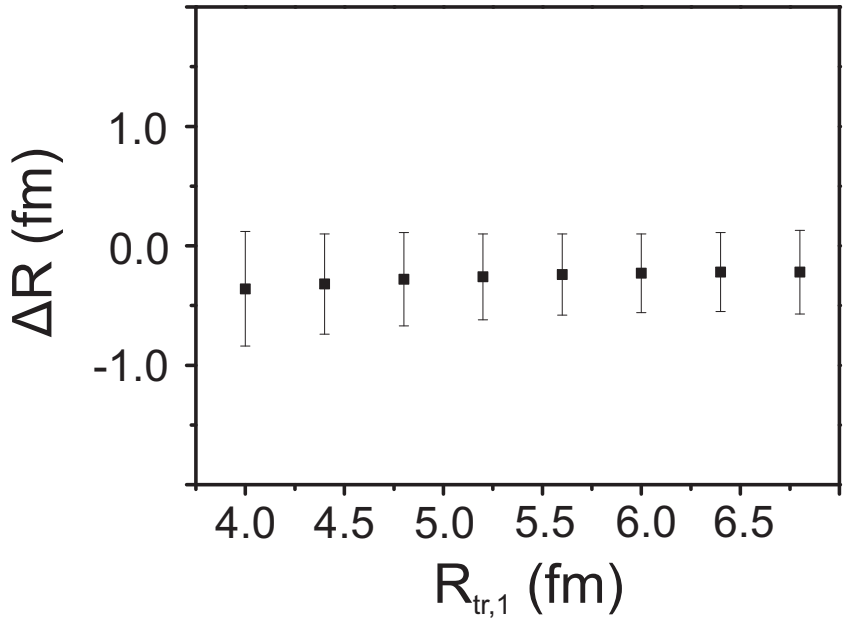

Figure 8.5: Evolution of the charge-transition radii difference between the 2_1^+ and 2_2^+ states in ^{94}Zr obtained from Eq. (7.12) as a function of the transition radius $R_{\mathrm{tr},1}$.

taken from the Ref [12]. It is thus particularly suited to test the applicability of the new PWBA analysis and the predicted relation between the signs of dominant proton and neutron configurations of FSSs and MSSs, respectively, and the difference of proton and neutron transition radii. The measured peak areas and the ratio of the kinematical functions $R_F(q)$ are summarized in Tab. 8.3.

Table 8.3: Peak areas of electroexcitation of the $2_{1,3}^+$ states in ^{94}Mo in units of counts and the ratio R_F of the $2_{1,2}^+$ kinematical functions defined in Eq. (7.11).

Θ	q^2 (fm^{-2})	2_1^+	2_3^+	R_F
93°	0.265	8496(154)	1708(67)	1.01717
117°	0.366	35896(357)	7628(133)	1.01699
141°	0.447	13781(165)	3209(92)	1.01626
165°	0.538	852(34)	211(17)	1.00928

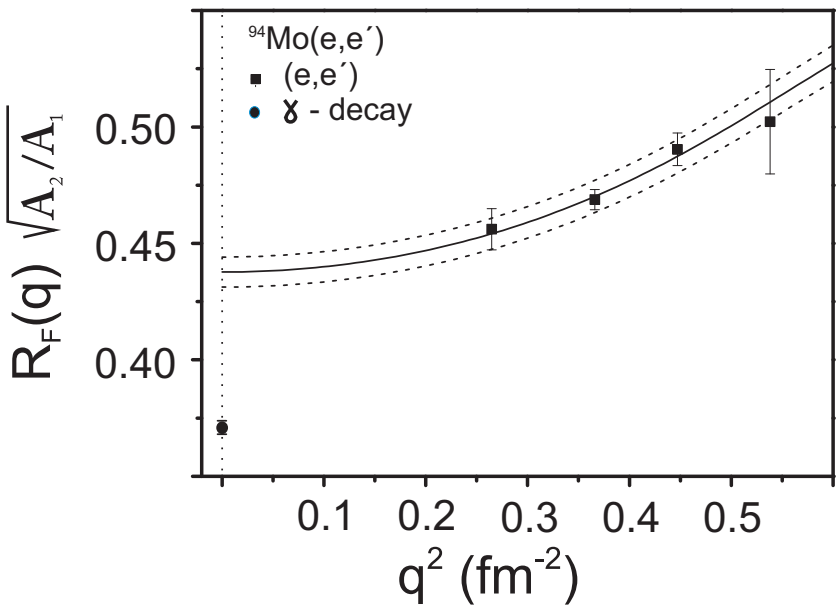

Figure 8.6: Ratio of the reduced transition probabilities of the 2^+ MSS and FSS (solid squares) of ^{94}Mo as a function of the squared elastic momentum transfer q_0. The solid line is a fit of Eq. (7.12) with 1σ error bars given by the dashed lines.

In this case, a χ^2-minimization of Eq.(7.12) to the data given in Tab 8.3 then determines $B(E2;2_2^+)/B(E2;2_1^+) = 0.192(1)$ which is in very good agreement with the value extracted from the QPM form factors scaled to the electron scattering data $B(E2;2_2^+)/B(E2;2_1^+) = 0.193(4)$ [12]. This ratio does not agree with Ref. [11] $B(E2;2_2^+)/B(E2;2_1^+) = 0.138(2)$ (see Fig. 8.6). The fit shows also a large non-zero $\Delta R = -0.75(12)$ fm.

In order to understand this result we need to investigate the momentum transfer dependence of the ratio of the Coulomb corrections of the 2_1^+ and 2_3^+ states. For this purpose the momentum transfer dependence of the form factor calculations in the Tassie model (section 7.2) have been adjusted to reproduce the experimental data as shown in Fig. 8.7: changing the parameter r_0 we obtained the correct position of the maximum of the form factor and the parameter ρ_0 to adjust the absolute value of the cross sections to data for both states. The extracted momentum transfer dependence of the form factors have been used to calculate the Coulomb corrections. As it is shown in Tab. 8.4 there is a clear momentum transfer dependence of R_F leading to a difference of more than 10% of the

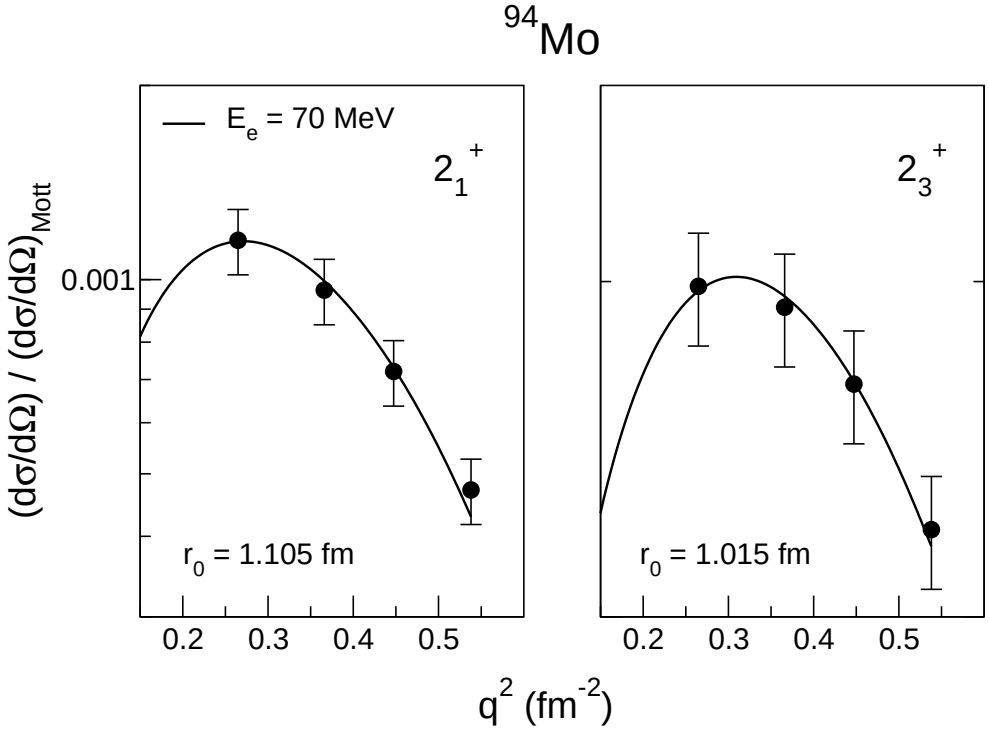

Figure 8.7: The momentum transfer dependence of the form factor in Tassie model (solid line) adjusted to the experimental data.

Table 8.4: Momentum transfer dependence of the individual states and of the ratio of the Coulomb corrections of the 2_1^+ and 2_3^+ states in ^{92}Mo deduced from the Tassie model

Θ	q^2 (fm^{-2})	$f_{C,2_1^+}$	$f_{C,2_3^+}$	R_F
93°	0.265	1.1617	1.2474	0.9816
117°	0.366	0.9367	1.0537	0.9589
141°	0.447	0.7458	0.8934	0.9285
165°	0.538	0.5471	0.7067	0.8880

highest measured momentum transfer. The ratio of Coulomb corrections factors thus needs to be included explicitly in the analysis. Indeed, a χ^2-minimization of Eq.(7.12) to the data given in Tab 8.3 including the ratio of the Coulomb corrections to the kinematic factor R_F leads to $B(E2;2_2^+)/B(E2;2_1^+) = 0.188(1)$ i.e., the deduced $B(E2)$ strength ratio hardly changed. The fit results, shown in

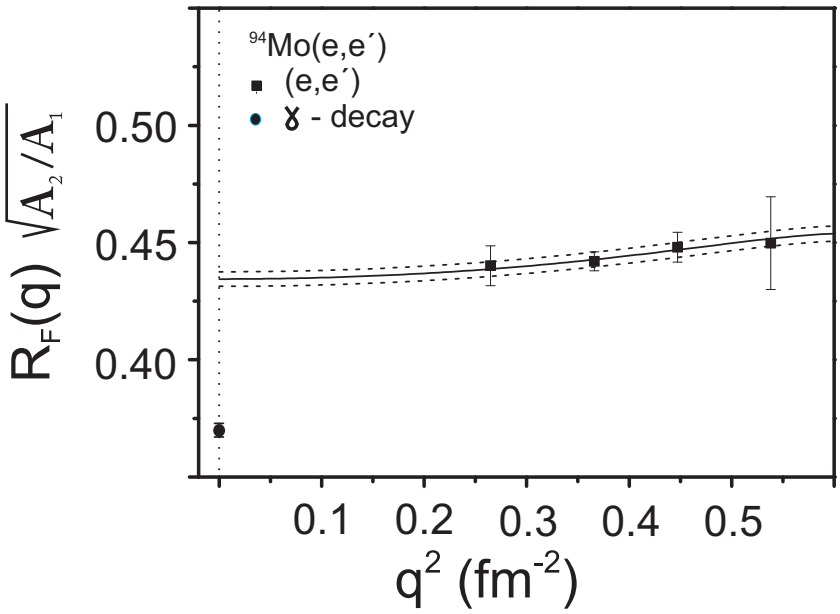

Figure 8.8: Ratio of the reduced transition probabilities of the 2^+ MSS and FSS (solid squares) of ^{94}Mo as a function of the squared elastic momentum transfer q_0. An additional point (full circle) at $q_0^2 = k^2$ stems from the ratio of $B(E2)$ strengths obtained from γ-decay lifetime measurements [11].The solid line is a fit of Eq. (7.12) with 1σ error bars given by the dashed lines.

Fig. 8.8, leads to a value $\Delta R = -0.13(5)$ fm which does not agree with 0.

8.4 Discussion of results

Summarizing the findings from the analysis of (e, e') data on 2^+ MSS in ^{92}Zr, ^{94}Zr and ^{94}Mo one can make the following observations:

(i) The ratio of $B(E2)$ strengths of MSS and FSS 2^+ states can be determined with high precision using the PWBA analysis introduced in Section 7. This is valid even if the assumption that the ratio of Coulomb corrections cancels at all momentum transfers does not hold. At the very small momentum transfer corresponding to the photon point ($q = E_x/\hbar c \approx 0.01$ fm^{-1}), the ratio of Coulomb corrections always approaches one although the corrections for the individual

transitions may be large.
(*ii*) For ^{92}Zr, the ratio of $B(E2)$ strengths to the 2^+ states is in a good agreement with the QPM predictions and with previous γ-decay lifetime measurements. The uncertainty of the $B(E2)$ value for the MSS is now limited by the experimental error bar for the $B(E2)$ strength to the 2_1^+ state.
(*iii*) The $B(E2)$ strength of the 2_2^+ state of ^{94}Zr is smaller than the $B(E2)$ value of the 2_1^+ state in contrast to the claim of [64] but in agreement with the result of Ref. [63]. Indeed, this anomaly has led to considerable discussion because it cannot easily interpreted in models successfully describing low-energy vibrations in heavy nuclei. Since both previous results have been obtained with the same experimental method, the independent confirmation of the result of Ref. [63] by the present data is of importance.
(*iv*) The $B(E2)$ ratio deduced from the $(e, e^{'})$ experiments differs from the literature value in ^{94}Mo. Since the $B(E2)$ strength to the MSS agrees with a γ-decay lifetime measurement [11], the problem must be in the data determining $B(E2; 2_1^+ \rightarrow 0_1^+)$. The available experimental results, mainly from Coulomb excitation, do show considerable scattering [77]. Thus, a new independent measurement of the $B(E2; 2_1^+ \rightarrow 0_1^+)$ value in ^{94}Mo data with an accuracy better than 30% is needed.
(*v*) In general, the accuracy of the new method is limited by the experimental knowledge on the $B(E2; 2_1^+ \rightarrow 0_1^+)$ strengths. Because many of the experiments determining $B(E2; 2_1^+ \rightarrow 0_1^+)$ values are quite old and show large scattering of results from different experiments [77], it provides a test of these values in cases where the $B(E2)$ value to the MSS is known from other data.
(*vi*) Proton transition radii differences in ^{92,94}Zr are compatible with zero within error bars. In Ref. [18], the relative sign of dominant proton/neutron components of the 2^+ state wave functions is related to the respective transition radii. The present result provides experimental confirmation of the microscopic prediction that in vibrational nuclei above the N = 50 shell closure the sign of proton components remains unchanged between FSS and MSS. The similarity confirms also the one-phonon picture of these symmetric and mixed-symmetry states.
(*vii*) In case of ^{94}Mo the assumption that Coulomb corrections cancel does not hold. At higher momentum transfer the deviation is non negligible, e.g. at $q^2 \approx 0.5$ fm^{-2} the ratio of the Coulomb corrections is about 0.89. However, this

dependence can be corrected within the Tassie model approach, where the applied Coulomb corrections do not depend on the detailed structure but the only assumption is collectivity.

The transition radii difference deduced in ^{94}Mo is more precise because of the very good statistics and the larger q range. The result, $\Delta R = -0.13(5)$ fm, differs from zero. In the model of Ref. [18] where transition densities are decomposed into leading two-quasiparticle and collective parts, a reduction of the transition radius of MSS with respect to FSS implies a shifting of the proton density to smaller radius R. Because the contribution of the two-quasiparticle component peaks at lower R compared to the collective part, such a result implies an increase of the proton two-quasiparticle amplitude in the wave function of the MSS.

9 Summary and outlook

The nature of one-phonon symmetric and mixed-symmetric 2^+ states in ^{92}Zr and ^{94}Zr has been investigated through inelastic electron scattering. Results from the QPM confirm the dominant one-phonon structure of the transitions to the first and second 2^+ state. Transition strengths are determined from a comparison of the experimental cross sections to the QPM results.

A new method for the extraction of the ratio of the $B(E2)$ strengths of the symmetric and mixed-symmetric 2^+ states and the charge transition radii differences between these states in vibrational nuclei from electron scattering data is introduced based on a PWBA analysis. It allows to extract the $B(E2)$ strengths ratio in the nuclei ^{92}Zr, ^{94}Zr and ^{94}Mo with high precision. It is demonstrated that this ratio is fully independent of the momentum transfer dependence of the Coulomb corrections for the two states.

The method also provides information on the difference of proton transition radii between MSS and FSS. According to the present results the differences of proton transition radii in ^{92,94}Zr are compatible with zero while a small deviation is observed in ^{94}Mo. In the interpretation of Ref. [18] the comparable proton transition radii difference of FSS and MSS confirms the microscopic prediction that the isovector character of the MSS arises from a sign change of the leading neutron quasiparticle components of the wave function, while the proton components remain essentially unchanged. For ^{94}Mo, the deviation from zero may be interpreted as a larger amplitude of the leading proton quasiparticle component in the MSS wave function.

In general, the present results demonstrate that in combination with experimental information on the neutron transition radii (derived e.g. from the matter transition radii measured in (p, p') experiments) one can test details of the quantum mechanical wave functions of the quadrupole low-energy structure in heavy nuclei. In order to establish the predicted new signature of MSS in this shell region experimental information on the neutron transition radii in ^{94}Zr is needed. Such data have been taken recently of iThemba LABS, and are presently analyzed. Further tests of the applicability when moving away from the $N = 50$ and $Z = 40$ shell closures are important. Candidates for such investigations are ^{96}Zr and ^{96}Ru.

References

[1] A. Arima, T. Otsuka, F. Iachello and I. Talmi, Phys. Lett. B**66**, 205 (1977).

[2] N. Pietralla, P. von Brentano and A. F. Lisetskiy, Prog. Part. Nucl. Phys. **60**, 225 (2008).

[3] A. Faessler, Nuclear Phys. **85** 653 (1966).

[4] N. Lo Iudice and F. Palumbo, Phys. Rev. Lett. **41**, 1532 (1978).

[5] D. Bohle, A. Richter, W. Steffen, A. E. L. Dieperink, N. Lo Iudice, F. Palumbo and O. Scholten, Phys. Lett. **B137**, 27 (1984).

[6] K. Heyde, P. von Neumann-Cosel and A. Richter, Rev. Mod. Phys. **82**, 2365 (2010).

[7] W.D. Hamilton, A. Irbäck and J.P. Elliott, Phys. Rev. Lett. **53**, 2469 (1984).

[8] F. Iachello, Phys. Rev. Lett. **53**, 1427 (1984).

[9] N. Pietralla, C. Fransen, D. Belic, P. von Brentano, C. Frießner, U. Kneissl, A. Linnemann, A. Nord, H. H. Pitz, T. Otsuka, I. Schneider, V. Werner, and I. Wiedenhöver, Phys. Rev. Lett. **83**, 1303 (1999).

[10] N. Pietralla, C. Fransen, P. von Brentano, A. Dewald, A. Fitzler, C. Frießner and J. Gableske, Phys. Rev. Lett. **84**, 3775 (2000).

[11] C. Fransen, N. Pietralla, Z. Ammar, D. Bandyopadhyay, N. Boukharouba, P. von Brentano, A. Dewald, J. Gableske, A. Gade, J. Jolie, U. Kneissl, S. R. Lesher, A. F. Lisetskiy, M. T. McEllistrem, M. Merrick, H. H. Pitz, N. Warr, V. Werner, and S. W. Yates,, Phys. Rev. **C67**, 024307 (2003).

[12] O. Burda, N. Botha, J. Carter, R. W. Fearick, S. V. Förtsch, C. Fransen, H. Fujita, J. D. Holt, M. Kuhar, A. Lenhardt, P. von Neumann-Cosel, R. Neveling, N. Pietralla, V. Yu. Ponomarev, A. Richter, O. Scholten, E. Sideras-Haddad, F. D. Smit, and J. Wambach, Phys. Rev. Lett. **99**, 029503 (2007).

[13] O. Burda, *Nature of Mixed-Symmetry* 2^+ *States in* ^{94}*Mo from High-Resolution Electron and Proton Scattering and Line Shape of the First Excited* $1/2^+$ *State in* ^{9}*Be*, Doctoral thesis D17, TU Darmstadt (2007).

[14] J. D. Holt, N. Pietralla, J. W. Holt, T. T. S. Kuo and G. Rainovski, Phys. Rev. C **76**, 034325 (2007).

[15] V. Werner, D. Belic, P. von Brentano, C. Fransen, A. Gade, H. von Garrel, J. Jolie, U. Kneissl, C. Kohstall, A. Linnemanna, A. F Lisetskiy, N. Pietralla, H. H Pitz, M. Scheck, K.-H Speidel, F. Stedile and S.W Yates, Phys. Lett. B**550**, 140 (2002).

[16] C. Fransen V. Werner, D. Bandyopadhyay, N. Boukharouba, S. R. Lesher, M. T. McEllistrem, J. Jolie, N. Pietralla, P. von Brentano, and S. W. Yates, Phys. Rev. C **71**, 054304 (2005).

[17] N. Lo Iudice and Ch. Stoyanov, Phys. Rev. C **73**, 037305 (2006).

[18] C. Walz, H. Fujita, A. Krugmann, P. von Neumann-Cosel, N. Pietralla, V. Yu. Ponomarev, A. Scheikh-Obeid, and J. Wambach, Phys. Rev. Lett. **106**, 062501 (2011).

[19] R. F. Casten, *Nuclear Structure from a Simple Perspective*, (Oxford University Press, New York, 2000).

[20] A. Arima und F. Iachello, Phys. Rev. Lett. **35**, 1069 (1975).

[21] D. Bonatsos, *Interacting Boson Models of Nucklear Structure*, Oxford University Press, Oxford, (1988).

[22] T. Otsuka, *Boson model of medium-heavy nuclei*, Ph.D. Thesis, University of Tokyo (1978).

[23] F. Iachello and A. Arima, *The Interacting Boson Model* (Cambridge University Press, Cambridge, 1987).

[24] A. Frank, J. Jolie and P. Van Isacker, *Symmetries in Atomic Nuclei* Springer Science+Business Media (2009).

[25] P. Van Isacker, K. Heyde, J. Jolie and A. Sevrin, Ann. Phys. (N.Y.) **171**, 253 (1986).

[26] A. Arima, F. Iachello, Ann. Phys. (NY) **99**, 253 (1976).

[27] A. Arima, F. Iachello, Ann. Phys. (NY) **111**, 201 (1978).

[28] A. Arima, F. Iachello, Ann. Phys. (NY) **123**, 468 (1979).

[29] F. Iachello, Nucl. Phys. A**358**, 89 (1981).

[30] P. Van Isacker, K. Heyde, J. Jolie and A. Sevrin, Ann. Phys. (NY) **171** (1986) 253.

[31] N. Pietralla, P. von Brentano, R. F. Casten, T. Otsuka and N. V. Zamfir, Phys. Rev. Lett. **73**, 2962 (1994).

[32] O. Otsuka, and K. H. Kim, Phys. Rev. C **50**, R1768 (1994).

[33] G. Siems, U. Neuneyer, I. Wiedenhöver, S. Albers, M. Eschenauer, R. Wirowski, A. Gelberg, P. von Brentano, T. Otsuka, Phys. Lett. **B320**, 1 (1994).

[34] N. Pietralla, P. von Brentano, T. Otsuka and R.F. Casten, Phys. Lett. **B349**, 1 (1995).

[35] N. Pietralla, T. Mizusaki, P. von Brentano, R.V. Jolos, T. Otsuka and V. Werner, Phys. Rev. C **57**, 150 (1998).

[36] Y.V. Palchikov, P. von Brentano and R.V. Jolos, Phys. Rev. C **57**, 3026 (1998).

[37] R.V. Jolos, Phys. At. Nucl. **64**, 465 (2001).

[38] V.G. Soloviev, *Theory of Atomic Nuclei: Quasiparticles and Phonons* (Inst. of Phys. Publ., Bristol and Philadelphia, 1992).

[39] A.I. Vdovin and V.G. Soloviev, Phys. Part. Nucl. **14**, 99 (1983).

[40] V.V. Voronov and V.G. Soloviev, Phys. Part. Nucl. **14**, 583 (1983).

[41] C. A. Bertulani and V.Yu. Ponomarev, Phys. Rep. **321** 251 (1999).

[42] A. Scheikh Obeid O. Burda, M. Chernykh, A. Krugmann, P. von Neumann-Cosel, N. Pietralla, I. Poltoratska,V. Yu. Ponomarev, and C. Walz, Phys. Rev. C **87**, 014337 (2013)

[43] H. Theissen, Springer Tracts in Mod. Phys. **65**, 1 (1972).

[44] T.W. Donnelly and I. Sick, Rev. Mod. Phys. **56** 461 (1984).

[45] A. Richter, *Operational Experience at the S–DALINAC*, Proc. of the 5$^{\text{th}}$ EPAC, Eds. S. Meyers, A. Pacheco, R. Pascual, C. Petit-Jean-Genaz and J. Poole, IOP Publishing, Bristol 110 (1996).

[46] R. Eichhorn, *Optimierung des Strahltransportsystems und experimentelle Umsetzung verschiedener Methoden zur Gütemesseung am S–DALINAC*, Doctoral thesis D17, TU Darmstadt (1999).

[47] P. von Neumann Cosel, F. Neumeyer, S. Nishizaki, V. Yu. Ponomarev, C. Rangacharyulu, B. Reitz, A. Richter, G. Schrieder, D. I. Sober, T. Waindzoch, and J. Wambach, Phys. Rev. Lett. **82**, 1105 (1999).

[48] B. Reitz, A. M. van den Berg, D. Frekers, F. Hofmann, M. de Huu, Y. Kalmykov, H. Lenske, P. von Neumann Cosel, A. Richter, G. Schreider, K. Schweda, J. Wambach, and H. J. Wörtche, Phys. Lett. **B532**, 179 (2002).

[49] N. Ryezayeva, *Search for the $p_{1/2^-}$ resonance in ^7H with the $^7Li(d,^2He)$ reaction and measurement of the deutron electrodisintegration under* 180° *at the S–DALINAC*, Doctoral thesis D17, TU Darmstadt (2006) .

[50] P. von Neumann Cosel, C. Rangacharyulu, A. Richter, G. Schrieder, A. Stascheck and S. Strauch, Phys. Rev. Lett. **78**, 2924 (1997).

[51] S. Strauch, P. von Neumann Cosel, C. Rangacharyulu, A. Richter, G. Schrieder, K. Schweda and J. Wambach, Phys. Rev. Lett. **85**, 2913 (2000).

[52] H. Diesener, U. Helm, P. von Neumann Cosel, A. Richter, G. Schrieder, A. Stascheck, A. Stiller and J. Carter, Nucl. Phys. **A696**, 272 (2001).

[53] P. von Neumann Cosel, A. Richter, G. Schrieder, A. Shevchenko, A. Stiller and H. Arenhövel, Phys. Rev. Lett. **88**, 202304 (2002).

[54] T. Walcher, R. Frey, H.-D. Gräf, E. Spamer and H. Theissen, Nucl. Instr. Meth **153**, 17 (1978).

[55] D. Schüll, J. Foh, H.-D. Gräf, H. Miska, R. Schneider, E. Spamer, H. Theissen, O. Titze and T. Walcher, Nucl. Instr. Meth. **153**, 29 (1978).

[56] J. Foh, R. Frey, R. Schneider, A. Schwierczinski, H. Theissen and O. Titze, Nucl. Instr. Meth. **153**, 43 (1978).

[57] H.-D. Gräf, H. Miska, E. Spamer, O. Titze and T. Walcher, Nucl. Instr. Meth. **153**, 9 (1978).

[58] S. Watzlawik, *Aufbau und Inbetriebnahme eines Strahlfhrungssystems fr hochauflösende Elektronenstreuexperimente am S-DALINAC*, Diploma thesis, TU Darmstadt (1999), unpuplished.

[59] A.W. Lenhardt, *Entwicklung einer Auslese-Elektronik für Silizium-mikrostreifenzaehler zum Einsatz als Detektor für minimalionisierende Elektronen am 169 Spektrometer des S-DALINAC*, Diploma thesis, TU Darmstadt (1999), unpublished.

[60] A.W. Lenhardt, *Entwicklung eines Si-Mikrostreifendetektors für das 169-Spektrometer am S-DALINAC*, Doctoral thesis D17, TU Darmstadt (2004).

[61] O. Burda, *Design of a shielding for the new focal plane detector system of the energy-loss spectrometer at the S-DALINAC*, Diploma thesis, Karazin Kharkiv National University, Ukraine,(2002), unpublished.

[62] W. Hartmann, GSI, Targetlabor (2012).

[63] A. Chakraborty, E. E. Peters, B. P. Crider, C. Andreoiu, P. C. Bender, D. S. Cross, G. A. Demand, A. B. Garnsworthy, P. E. Garrett, G. Hackman, B. Hadinia, S. Ketelhut, Ajay Kumar, K. G. Leach, M. T. McEllistrem, J. Pore, F. M.Prados-Estvez, E. T. Rand, B. Singh, E. R. Tardiff, Z.-M. Wang, J. L. Wood and S. W. Yates, Phys. Rev. Lett. **110**, 022504 (2013).

[64] E. Elhami, J. N. Orce, M. Scheck, S. Mukhopadhyay, S. N. Choudry, M. T. McEllistrem, S. W. Yates, C. Angell, M. Boswell, B. Fallin, C. R. Howell, A. Hutcheson, H. J. Karwowski, J. H. Kelley, Y. Parpottas, A. P. Tonchev, and W. Tornow, Phys. Rev. C **78**, 064303 (2008).

[65] S. Strauch, *Computer program FIT*,Diploma thesis, TH Darmstadt (1993), unpublished.

[66] F. Neumeyer, *Computer program FIT*,Diploma thesis, TH Darmstadt (1993), unpublished.

[67] H. Überall, *Electron Scattering From Complex Nuclei - Part A*, Academic Press, New York - London (1971).

[68] L. C. Maximon and D.B. Isabelle, Phys. Rev. **B113**, 193 (1964).

[69] L. C. Maximon, Rev. Mod. Phys. **41**, 1344 (1969).

[70] L. W. Mo and Y. S. Tsai, Rev. Mod. Phys. **41**, 205 (1969).

[71] V. Werner, N. Benczer-Koller, G. Kumbartzki, J. D. Holt, P. Boutachkov, E. Stefanova, M. Perry, N. Pietralla, H. Ai, K. Aleksandrova, G. Anderson, R. B. Cakirli, R. J. Casperson, R. F. Casten, M. Chamberlain, C. Copos, B. Darakchieva, S. Eckel, M. Evtimova, C. R. Fitzpatrick, A. B. Garnsworthy, G. Gürdal, A. Heinz, D. Kovacheva, C. Lambie-Hanson, X. Liang, P. Manchev, E. A. McCutchan, D. A. Meyer, J. Qian, A. Schmidt, N. J. Thompson, E. Williams, and R. Winkler, Phys. Rev. **C78**, 031301 (2008).

[72] T. Kibedi and R. H. Spear, At. Data Nucl. Data Tables **80**, 35 (2002).

[73] G. Jakob, N. Benczer-Koller, J. Holden, G. Kumbartzki, T.J. Mertzimekis, K.-H. Speidel, C.W. Beausang and R. Krücken, Phys. Lett. B**468**, 140 (1999).

[74] V. Yu. Ponomarev, private comunication.

[75] J. Heisenberg and H. P. Blok, Annu. Rev. Nucl. Part. Sci. C **33** 0569 (1983).

[76] L. J. Tassie, Austr. J. Phys. **9**, 407 (1956).

[77] S. Raman, C.W. Nestor,Jr., and P. Tikkanen, At. Data. Nucl. Data Tables **78** 1 (2001).

Danksagung

An dieser Stelle möchte ich mich herzlich bei allen bedanken, die mir bei der Fertigstellung dieser Arbeit mit Rat und Tat beigestanden haben, und ohne deren Unterstützung und Hilfsbereitschaft sie nicht zustande gekommen wäre.

An erster Stelle gilt mein Dank Herrn Professor Norbert Pietralla, der mir die Möglichkeit gab, an der Technischen Universität Darmstadt zu promovieren. Sein großes Interesse und seine Unterstützung in jeder Hinsicht, die mich während meiner Promotion begleiteten, haben wesentlich zum Erfolg dieser Arbeit beigetragen. Er hat es mir ermöglicht, an Workshops und Konferenzen teilzunehmen. Dies hat meine Sichtweite entscheidend erweitert und war eine wichtige und wertvolle Erfahrung für mich.

Herrn Professor Peter von Neumann Cosel danke ich für die Übernahme des Korreferats. Er hat mir in allen Phasen der Promotion mit Rat und Tat geholfen. Er war immer ein ständiger und wichtiger Ansprechpartner. Dafür möchte ich mich ganz herzlich bedanken.

I am very grateful to Dr. V. Yu. Ponomarev for providing me with QPM and Tassie model calculations and for his support in helpful discussions, suggestions and the theoretical interpretations of the experimental results.

Allen Mietgliedern der Beschleunigergruppe des S-DALINAC danke ich für die Bereitstellung eines exzellenten Strahls. Ein besonderer Dank gilt Herrn Dr. F. Hug, S. Sievers, Dr. R. Eichhorn und Dr. M. Konrad

Bei meinen früheren Kollegen und allen derzeitigen Mitarbeitern der Spektrometer-Gruppe, insbesondere Dr. L. Coquard, Dr. O. Burda, S. Rathi, S. Aslanidou, J. Birkhan, A. Krugmann, A. M. Krumbholz und B. Bozorgian möchte ich mich für die Hilfe und für die gute Zusammenarbeit bedanken.

Ganz großer Dank geht an meinen Bruder Modar Sheikh Obeid. Ohne seine Unterstützung war es mir nicht möglich mein Studium fortzuführen. Seine brüderliche Freundschaft bedeutet mir unbeschreiblich viel. Herzlichen Dank fr jede Unterstützung und den großen Beistand, den er jederzeit zu geben bereit ist.

Meiner lieben Frau Sawamer Alsayed danke ich für ihr Verständnis und ihre Unterstützung. Sie hat mir immer den Rücken freigehalten und unsere drei schönen Töchter fast allein erzogen.

Meinem besten Freund Mohamad Al-Ahmad danke ich aus ganzem Herzen für seine Freundschaft, die er niemals aufgegeben hat.

Den größten Dank schulde ich meinen Eltern, Mohamad Scheikh Obeid und Fatema Alsayed, die mir stets die Freiheit gelassen haben, meine eigenen Wege zu gehen und mir in meinem Leben zu jedem Zeitpunkt mit Rat und liebevoller Unterstützung bedingungslos zur Seite standen.

Die vorliegende Arbeit wurde gefördert durch Mittel der DFG im Rahmen des Sonderforschungsbereiches SFB 634 "Kernstruktur, nukleare Astrophysik und fundamentale Experimente bei kleinen Impulsüberträgen am supraleitenden Darmstädter Elektronenbeschleuniger S-DALINAC".

LEBENSLAUF

Abdulrahman Scheikh Obeid

3. Oktober 1974	Geboren in Damaskus, Syrian
1980 – 1986	Besuch der Grundschule in Barza-Damaskus
1986 – 1989	Besuch der Gesamtschule in Mesyaf-Syrian
1989 – 1992	Besuch der Gymnasium in Mesyaf-Syrian
Juli 1993	Abitur
1994 – 2000	Studium der Physik an der Universität Aleppo
September 2000	Diplom in Physik; Abschluss des Studiums
2000 – 2002	Grundwehrdienst in Aleppo, Syrian.
2004 – 2006	Studium der Physik an der Universität Potsdam
Dezember 2006	Diplom in Physik; Abschluss des Studiums
seit März 2007	Wissenschaftlicher Mitarbeiter am Institut für Kernphysik der Technischen Universität Darmstadt
Juni 2013	Doktor in Physik; Technische Universität Darmstadt

Eidesstattliche Erklärung:

Hiermit erkläre ich, daß ich die vorliegende Dissertation selbständig verfaßt, keine anderen als die angegebenen Hilfsmittel verwendet und bisher noch keinen Promotionsversuch unternommen habe.

Darmstadt, den 21. Mai 2013

Abdulrahman Scheikh Obeid